2012

Robustness of speckle imaging techniques applied to horizontal imaging scenarios

Jeremy P. Bos
Michigan Technological University

ROBUSTNESS OF SPECKLE IMAGING TECHNIQUES APPLIED TO HORIZONTAL IMAGING SCENARIOS

By

Jeremy P. Bos

A DISSERTATION

Submitted in partial fulfillment of the requirements for the degree of

DOCTOR OF PHILOSOPHY

(Electrical Engineering)

MICHIGAN TECHNOLOGICAL UNIVERSITY

2012

This dissertation, "Robustness of Speckle Imaging Techniques Applied To Horizontal Imaging Scenarios ," is hereby approved in partial fulfillment of the requirements for the Degree of DOCTOR OF PHILOSOPHY IN ELECTRICAL ENGINEERING.

Department of Electrical and Computer Engineering

Signatures:

Dissertation Advisor _____
Dr. Michael C. Roggemann

Committee Member _____
Dr. Christopher Middlebrook

Committee Member _____
Dr. Timothy Schulz

Committee Member _____
Dr. Alan Struthers

Department Chair _____
Dr. Dan Fuhrmann

Date _____

To my wife Jessica, my parents, family, friends, and colleagues.

Contents

List of Figures

List of Tables

Preface

This dissertation is mainly comprised of three journal articles authored by my advisor, Dr. Michael Roggemann, and myself. The first article appears in Chapter 2 was published online [1] on May 15, 2012 and is scheduled to appear in print in the October issue of Optical Engineering as "A technique for simulating anisoplanatic image formation over long horizontal paths". Dr. Roggemann is listed as a contributing author on this paper as he provided the original idea for simulation technique and help me develop the paper. As first author, I performed all other contributing work and wrote and prepared the manuscript. The content of Chapter 3 is sourced from "Robustness of speckle imaging techniques applied to horizontal imaging scenarios" [2]. This paper was written and prepared by myself and edited by my advisor. Dr. Roggemann also provided MATLAB code that I later modified for recovering the bispectrum. I developed all code used for computing the cross spectrum or the Knox-Thompson recovery method and the parametric analysis included in the paper. The final paper appears as submitted to Optical Engineering in Chapter 4, I performed all work and prepared all portions of this chapter with revisions provided by my advisor. The field data used in this paper was also provided by my advisor. Though the work and contributions to field presented in this work are my own their completion and publication would not have been possible without my advisors feedback and recommendations for improvement.

Acknowledgments

There is a long list of people who deserve recognition for helping me reach this point in my career and subsequently completing this work. First and foremost, this work would not have been possible without the generous support and guidance of my advisor Dr. Michael Roggemann; I feel extremely fortunate having been his advisee. My wife Jessica also deserves recognition for the countless hours she spent proofreading endless drafts of conference papers, journal articles and chapters that eventually became this dissertation. Thanks also goes out to my committee for their time and helpful suggestion in improving my research. Finally, I want to take space here to thank Michigan Technological University and the surrounding community, alumni, and staff who support this institution, for the opportunities they have created for me throughout my career and into the future.

Abstract

Atmospheric turbulence near the ground severely limits the quality of imagery acquired over long horizontal paths. In defense, surveillance, and border security applications, there is interest in deploying man-portable, embedded systems incorporating image reconstruction methods to compensate turbulence effects. While many image reconstruction methods have been proposed, their suitability for use in man-portable embedded systems is uncertain. To be effective, these systems must operate over significant variations in turbulence conditions while subject to other variations due to operation by novice users. Systems that meet these requirements and are otherwise designed to be immune to the factors that cause variation in performance are considered robust. In addition robustness in design, the portable nature of these systems implies a preference for systems with a minimum level of computational complexity.

Speckle imaging methods have recently been proposed as being well suited for use in man-portable horizontal imagers. In this work, the robustness of speckle imaging methods is established by identifying a subset of design parameters that provide immunity to the expected variations in operating conditions while minimizing the computation time necessary for image recovery. Design parameters are selected by parametric evaluation of system performance as factors external to the system are varied. The precise control necessary for such an evaluation is made possible using image sets of turbulence degraded

imagery developed using a novel technique for simulating anisoplanatic image formation over long horizontal paths. System performance is statistically evaluated over multiple reconstruction using the Mean Squared Error (MSE) to evaluate reconstruction quality. In addition to more general design parameters, the relative performance the bispectrum and the Knox-Thompson phase recovery methods is also compared.

As an outcome of this work it can be concluded that speckle-imaging techniques are robust to the variation in turbulence conditions and user controlled parameters expected when operating during the day over long horizontal paths. Speckle imaging systems that incorporate 15 or more image frames and 4 estimates of the object phase per reconstruction provide up to 45% reduction in MSE and 68% reduction in the deviation. In addition, Knox-Thompson phase recover method is shown to produce images in half the time required by the bispectrum. The quality of images reconstructed using Knox-Thompson and bispectrum methods are also found to be nearly identical. Finally, it is shown that certain blind image quality metrics can be used in place of the MSE to evaluate quality in field scenarios. Using blind metrics rather depending on user estimates allows for reconstruction quality that differs from the minimum MSE by as little as 1%, significantly reducing the deviation in performance due to user action.

Chapter 1

Introduction

Scenarios where imaging systems are tasked with acquiring information about remote objects over long horizontal paths are common to defense, border enforcement, and surveillance applications. In these scenarios, the presence of atmospheric turbulence along the imaging path corrupts acquired imagery. A variety of image reconstruction methods have been proposed and are currently being developed to counteract turbulence effects in these scenarios. However, incorporating these methods into a man-portable embedded imaging system introduces a number of severe design constraints that complicated system design. Specifically, these systems are often carried to an observation site implying strict limitations on Size, Weight, and Power (SWaP). Minimizing SWaP in embedded systems implicitly requires that the system have the lowest possible computational complexity. In addition, to be practical, these methods must provide high quality imagery over a range of

turbulence conditions and variations in external parameters, including interaction by users. In the language of product development engineering, systems that meet these requirements are referred to as “robust”.

Speckle imaging systems are already recognized as being computationally efficient compared to many of the methods proposed for horizontal imaging, though they have not been shown to be robust. The aim of this work is to show that speckle image reconstructions methods are robust to variation in external and user-controlled parameters. Further, I aim to identify a subset of design parameters that result in high quality image reconstructions at the lowest possible computation burden. It is hoped that this work will assist in the development of embedded systems incorporating speckle imaging techniques and provide a template for the evaluation of other methods.

1.1 Design for Robustness

The idea of robustness in engineering design was pioneered by Taguchi [3] who defined robustness as being immune to the factors that cause variability in performance. Incorporating robustness into product design first requires identifying a suitable quality metric, and then all of the factors that affect product quality. Factors external to the system are referred to as “noise” parameters, while those that are controlled by the designer are referred to as “design” parameters. In a complete robustness analysis, noise and design

parameters are varied over their expected range of variation and the quality, or performance, recorded. This process identifies the design parameters that most affect system performance and identifies optimum values for each parameter.

In Taguchi's original work on robustness, quality was evaluated using a loss function, which he developed. Since this early work, a number of other loss functions have been proposed. While these metrics may differ in their purpose, they are generally related to the Signal to Noise Ratio (SNR). In this work, the Mean Squared Error (MSE) in normalized intensity value per pixel of the system output relative to a diffraction-limited reference image will be used to evaluate quality. When properly normalized, the MSE is equivalent to the inverse of the SNR. Therefore, the goal of this work will be to identify a set of design parameters that provides the Minimum Mean Squared Error (MMSE) performance at the lowest level of computational complexity. In the following sections I briefly describe speckle imaging and identify important design and noise parameters. Descriptions of the conditions identified as horizontal imaging scenarios and relevant noise parameters are also found in subsequent sections.

1.2 Speckle Imaging

Speckle imaging has been used in the imaging of space objects from ground-based observatories for over 40 years. Labeyrie [4] first recognized that high frequency spatial

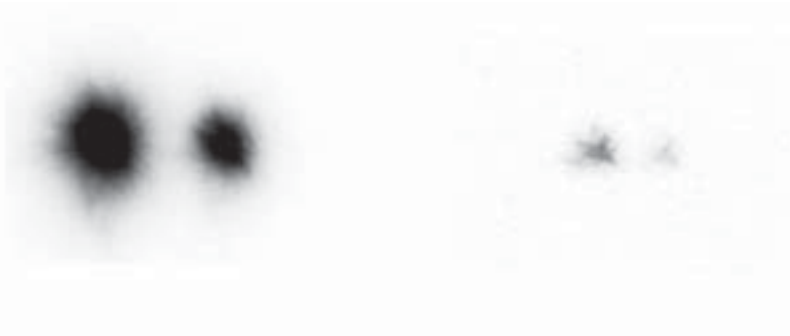

Figure 1.1: Long-Exposure (left) and short-exposure image (right) of the visual binary stars Alcor and Mizar in the Ursa Major.

information was retained in short-exposure images of bright stars. In Fig.1.1, the long-exposure and short-exposure of a visual binary star are compared. The long-exposure image on the left of the figure demonstrates the blurring that reduces the detail in images acquired through turbulence. The image on the right is affected by the same turbulence conditions, but at short exposures, is seen to contain fine detail by way of multiple bright patches or speckles. Labeyrie found that the size of these speckles is on the order of the diffraction-limit of the imaging system. To recover information about the object Labeyrie used a Fourier transforming lens to capture the amplitude spectrum from multiple short exposures on a roll of film. The developed film was then played back and exposed onto a slide over one long exposure. The resulting image effectively displayed the uncorrupted Power Spectral Density (PSD) of the object. While this technique was useful in recovering simple geometric information, such as the separation of binary stars, it does not provide the phase information necessary for image recovery.

In the years following Labeyrie's experiments a number of phase recovery techniques were proposed, many based on interferometric imaging techniques used by radio astronomers. The two most popular methods used in speckle imaging rely on phase recovery from ensemble averages of certain high order statistical quantities. One technique, originally proposed by Knox and Thompson [5], relies on the image cross-spectrum, the frequency domain equivalent of the object-intensity cross-correlation, for phase recovery. Weigelt [6] later proposed using the bispectrum, or the Fourier transform of the triple correlation for the same purpose. Since that time, the bispectrum has won favor for use in astronomical imaging. Using the bispectrum is desirable because it is shift-invariant and provides superior reconstruction quality at lower signal-to-noise ratios. All of the proposed phase recovery methods rely on recursive recovery of the object phase using high-order statistics of the object spectrum. Due to the inherent computational complexity of these operations, significant computer time was necessary to recover useful imagery. Consequently, practical use of speckle imaging was limited to research labs with access to supercomputing resources.

The advent of affordable, high performance computing workstations in the 1990s led to a great deal of research regarding speckle imagers and their performance limitations relative to the imaging of space objects [7], [8], [9]. In these scenarios, imaging is generally photon-limited requiring many thousands of frames acquired over many hours to generate a single image. In addition, it was generally assumed the object of interest was imaged within a field of view smaller than the isoplanatic angle of the atmosphere. The object

is also assumed to exist against a flat background providing limited support. Using these assumptions allowed for a comprehensive analysis of the performance of speckle imaging techniques as a function of input SNR. This period also provided improved methods of phase recovery from bispectrum by researchers such as Meng [10] and Matson [11].

Recently, there has been a renewed interest in applying speckle imaging techniques to horizontal imaging scenarios [12]. However, the simplifying assumptions used to characterize speckle imaging in the imaging of space objects do not necessarily apply in the horizontal imaging case. Specifically, objects are likely to span multiple isoplanatic patches and therefore experience non-uniform tip and tilt distortions. In these circumstances, the linear system framework used to evaluate system performance analytically does not apply. While it is possible to make heuristic arguments that analytic results for speckle imaging performance remain valid under these anisoplanatic conditions, there is little, if any, empirical evidence to support this argument. Images obtained in horizontal imaging are also not likely to be photon-starved, although additive noise may be present in the acquired imagery. In either case, turbulence strength, not per frame SNR is likely to limit performance. Further, the importance of computation complexity and reconstruction rate requires a change in focus. Rather than focusing only on image quality it is also valuable to understand how few frames are required to provide acceptable reconstructions.

1.3 Horizontal Imaging

Uneven heating of the ground by the sun results in temperature inhomogeneities in the near-surface air mass. Large-scale temperature differences in the air mass are resolved by the flow of air along pressure gradients. Due to the low viscosity of air, this movement generates turbulent eddies with characteristic scale sizes on the order of the inhomogeneities. As they flow, these eddies diffuse, breaking into smaller and smaller eddies and eventually dissipating via molecular friction and increasing the temperature in the air mass. During the daytime, the Sun continually supplies energy to this process increasing the turbulence strength near the ground over the course of the day. Overall turbulence severity reaches a peak shortly after midday and then decreases to a minimum after sunset when the rate of Turbulent Kinetic Energy (TKE) generation via solar heating is exceeded by the dissipation due to molecular friction. After sundown, turbulence near the ground is less predictable with relative periods of strong and weak turbulence attributable to synoptic-scale events in the troposphere. Near-ground turbulence conditions remain unstable until solar heating returns with dawn generating another stable turbulence minimum after which the diurnal turbulence process repeats.

The presence of turbulence near the ground affects light propagation by randomly refracting light as it travels through the air volume. The same temperature differences that generate flow of the air mass and turbulence also create randomly distributed differences in the

index of refraction. The deviation in refractive index is small but, when accumulated over long enough paths, can have deleterious effects on imaging systems. It is common to model the turbulence volume between the light source and the imager as a random medium and modeled such that the distribution of energy at various turbulence scale sizes reduces logarithmically from large, or outer scale, inhomogeneities down to the inner scale where molecular viscosity dominates. Mediums that conform to this model are referred to as power-law media and, in the case where the roll-off in TKE in terms of wavenumber between these two ranges follows a $-\frac{11}{3}$ slope [13], the medium is referred to as a Kolmogorov medium. The spatial distribution of TKE can be directly related to variations the index of refraction in air, allowing analysis of the effect of atmospheric turbulence on light wave propagation.

The effects of wave propagation through random media on imaging systems is traditionally modeled as random phase perturbations to the wavefront phase. Fully characterizing the effects of turbulence on light wave propagation requires solving the stochastic Hemholtz equation. Analytic approaches often rely on a series of simplifying assumptions to make a solution tractable. First, the medium is assumed to be homogeneous in as much that it has the same turbulence properties (i.e. Kolmogorov medium) throughout the volume. Next, the medium is generally assumed to be isotropic along the direction of propagation. Turbulence strength is also assumed to be weak enough that scintillation effects can be ignored. These two assumptions are often referred to collectively as the Rytov approximation. Relative to the problem considered in this work, it is also common

to assume the turbulence strength along the imaging is roughly dependent upon the height above the ground [14]. Because of this dependence, the turbulence strength along the imaging path can be assumed to be constant for the purely horizontal and slightly slanted paths of interest in this work. An alternative to purely analytic approaches is the use of wave propagation simulations incorporating random phase screens with Kolmogorov spatial statistics. In particular, the Fourier split-step propagation method is known [15], [16], [17] to provide an excellent match to experimental data. Though numerical simulations are often used in place of analytical models, many of the same assumptions (the Rytov approximation in particular) are still applied.

1.4 Approach

In this dissertation, I propose establishing the robustness of speckle imaging methods by parametric evaluation of system performance as design parameters and noise factors are varied. The system design parameters relevant here are:

- N_f - Number of input frames used to produce each image reconstruction.
- N_p - Number of estimates of the object phase at each spatial frequency, $\vec{f}$, in the estimated object spectrum $\hat{O}(\vec{f})$

- The method used for object phase recovery. Both the bispectrum and Knox-Thompson methods are evaluated.

- α - The Weiner filter noise parameter. α is a SNR dependent parameter in the denominator of the pseudo-Weiner filter used for object recovery. Though the parameter is technically SNR dependent, it is common to tune this parameter to produce the highest quality image.

The external noise factors are:

- Turbulence strength - System performance is evaluated as turbulence strength is varied over a range of turbulence strengths that produce "Low", "Moderate" and "Severe" image degradation.

- Estimate of C_n^2 - Image recovery in speckle imaging systems requires deconvolution via a pseduo-Weiner filter of the estimate object amplitude spectrum using an estimate of the long exposure atmospheric Optical Transfer Function (OTF), H_{LE}. A proven theoretical model for H_{LE} [18] which is dependent on the distribution of turbulence strength along the imaging path is often used for this purpose. After, applying the assumptions of constant turbulence strength and assuming the imaging path length, L, is known an estimate of the turbulence strength in terms of the refractive index structure constant, C_n^2 is still required. It is assumed that either the user, or the imaging system, are able estimate turbulence strength within an order of

magnitude of the true value and examine the sensitivity in system performance over this range.

- σ_n - System performance is evaluated with various levels of additive Gaussian noise added to input image frames.

The controlled conditions necessary to perform a parametric evaluation are enabled by the development of a method for simulating anisoplanatic image formation through turbulence over long horizontal paths. This method is used to generate 3 sets of 1000 turbulence corrupted image frames. The size of this data set allows for statistically significant evaluation of system performance over at least $N = 20$ independent speckle image reconstructions $N_f = 50$ input frames. In this work, system performance is evaluated in terms of the MSE. The subset of parameters that result in the MMSE while minimizing image reconstruction time will be identified as optimum.

A significant potential source of variation in the performance of speckle imaging systems is the selection of the atmospheric OTF used for object amplitude recovery. This work makes use of a well established theoretical model for the atmospheric OTF with a single free parameter in C_n^2. Using our simulated data set it trivial to choose a value of C_n^2 that results in the highest quality image reconstruction. In the field, this parameter must be estimated by the user; a difficult task even for experts. To address this issue the simulated data set is used to compare the response of certain Blind Image Quality (BIQ) metrics to the MSE. After establishing a baseline using simulated imagery, the BIQ metrics are applied to field

imagery acquired during a recent Laser Communication System (LCS) Experiment [19].

1.5 Summary of Key Results

In this dissertation, the robustness of speckle imaging systems is evaluated in horizontal imaging scenarios by parametric evaluation of the system design and noise parameters that affect performance. This evaluation is enabled by the invention of a new method for simulating image formation over long horizontal paths. It is shown that this method can be validated to theoretical models for turbulence effects on imaging. In addition, images simulated using this method contain the anisoplanatic distortions found in most imagery acquired over horizontal imaging paths. The simulation model is used to generate a 3000-frame data set based on the"Lena" test image. The distribution of MSE counts across image frames in the data set is log-normally distributed with a mean value that increases approximately linearly with turbulence strength over the range examined.

Parametric evaluation of speckle imaging performance is achieved by variation of the system design and noise parameters detailed Section 1.4 using frames from the data set as input frames. Performance statistics are measured for at least $N = 20$ reconstructions for three levels of turbulence-induced image degradation. On average, across the three conditions, the MSE of reconstructed image frames improved 48% compared to the input data set and the deviation about the mean decreased by 68%. Further, performance near the

limit available from speckle imaging methods is available using only, $N_f = 15$ input frames and $N_p = 4$ phase estimates per spatial frequency. In addition, the performance of the Knox-Thompson method of phase recovery is shown to be equivalent to the bispectrum method in horizontal imaging scenarios. Finally, it is shown that using the true value of simulated turbulence strength in the inverse filter used for object amplitude recovery does not guarantee the highest quality reconstructions. While poor estimates do result in sub-optimal reconstruction, there is generally a wide range of values over which there is little variation in performance.

Design engineers can set most of the design parameters evaluated here before the system reaches the user. The one exception is the estimate of C_n^2 used for object amplitude recovery. Though performance is rather insensitive to small variations in this parameter, poor estimates can significantly degrade image quality. Using the MSE, and simulated imagery, it is a trivial task to tune this value to its optimum; in the field, however, such tuning is not possible. To overcome this limitation, two BIQ metrics are evaluated for use as practical surrogates to the MSE. It is shown that both metrics are capable of producing imagery that is subjectively identical to the MMSE image. Images chosen as optimum by the blind metrics differ from the MMSE image by less than 4% on average.

1.6 Organization

The remainder of this dissertation is comprised of content from three journal articles which have either been accepted for publication or under review by the editors of SPIE Optical Engineering. Changes to formatting and language in the articles have been made where appropriate. Chapter 2 is derived from "Technique for Simulating Anisoplanatic Image Formation Over Long Horizontal paths" [1] which was published online on May 15, 2012 in Optical Engineering. This paper provides an overview of the horizontal imaging problem and the method used to develop the data set of simulated imagery used for the parametric analysis described in Chapter 3. The content in Chapter 3 has been appears in the August 2012 issue of Optical Engineering as "Robustness of Speckle Imaging Techniques Applied to Horizontal Imaging Scenarios" [2]. Evaluation of BIQ to the task providing optimal imagery recovered using speckle imaging methods is found in Chapter 4. The content in Chapter 4 was submitted to Optical Engineering on June 28,2012 under the title "Blind Image Quality Metrics for Optimal Speckle Image Reconstruction in Horizontal Imaging Scenarios." A conclusion summarizing the findings in this body of work, and providing guidance for further research are found in Chapter 5.

Chapter 2

A Technique for Simulating Anisoplanatic Image Formation Over Long Horizontal Paths

[1]

[1]The material contained in this chapter was previously published in the journal Optical Engineering published online on May 15, 2012 [1] and is scheduled to appear in print in the October 2012 issue of the journal. See Appendix C for documentation of permission to republish this material.

2.1 Introduction

In signal processing problems, recovery methods are commonly evaluated by simulation of the noise or distortion process applied to a known signal. The performance of a reconstruction method can be evaluated by direct comparison of the estimator output to the known input. Similarly, robustness can be evaluated by examining the variation in performance over a range of noise conditions. Extending this evaluation process to image processing problems involving the observation of space objects though turbulence is straightforward. Simulation methods [18] are well established and available commercial software makes simulating a range of conditions trivial–but only under isoplanatic conditions. Unfortunately, the isoplanatic assumption used to simplify simulation in these circumstances does not generally apply to imaging over horizontal paths. In order to evaluate the image reconstruction methods applied to the horizontal imaging problem a different simulation method is needed.

The aim in developing a simulation model specific to horizontal imaging is to evaluate the ability of past, present and future image reconstruction techniques to recover images of scenes corrupted by turbulence featuring severe anisoplanatic distortions. Most image reconstruction techniques used to compensate for atmospheric distortions, such as multi-frame blind deconvolution and speckle imaging techniques, make use of multiple frames to produce a single recovered image. Therefore, in order to effectively evaluate

these techniques any simulation tool must reproduce horizontal imaging conditions over many frames and under controlled conditions. A certain level of efficiency is also desired if we are to generate enough frames to provide a level of statistical certainty in the performance of these estimators.

The need for an absolute prior rules out the use of data collected in the field as a substitute for simulation and previous attempts at modeling anisoplanatic conditions do not provide the level of fidelity required. For example, Vorontstov [20] successfully produced anisoplantatic effects using in the laboratory using a series of heaters placed between a scene and an imaging system. Many images exhibiting anisoplanatic distortions can be quickly acquired using this method and a truth object can be acquired by simply removing the heating elements. While these images do contain severe anisoplanatic distortions the turbulence is not guaranteed to be isotropic or homogenous resulting in fluctuation non-Kolmogorov fluctuation statistics.

Carrano [21] developed a computer simulation method that began with an image represented as a series of discrete sources with amplitude values derived from the object intensity distribution and with uniformly distributed independent random phase values assigned to each source. The complex field is propagated through the atmosphere and turbulence effects introduced by phase screens placed along the imaging path. The result of a single propagation using this method is a noise-dominated, speckled, intensity image. To produce a fully formed image with sufficiently high signal-to-noise ratio

requires summation over several thousand speckle frames. In addition to the computation time required, the presence of the random phase noise introduced by this method is undesirable; the preference being to analyze noise effects independently. This same work [21] introduces a method similar to the one presented here to create images of point sources. However, this method makes use of a single screen and does not fully reproduce both the anisoplanatic and seeing effects associated with the complete turbulence volume.

The method described in this paper is a simplification of the split-step method [22] originally used to model the propagation of acoustic waves in underwater channels. This method has since been extended to the simulation of light propagation through the atmosphere [16],[15]. The approach taken here divides the simulated object into blocks or patches smaller than the isoplanatic angle of the imaging system. As in other methods, the atmosphere is simulated by a series of phase screens placed along the imaging path. Propagation is approximated using geometrical optics to accumulate the phase perturbations resulting from each screen. The accrued phase distortions are combined with the unperturbed phase resulting from spherical wave propagation from the object to the imaging aperture. These phase errors are used to develop a point spread function (PSF) specific to each block-source in the object. These PSFs are then normalized, ignoring scintillation, and scaled by an intensity value sampled from the object intensity distribution. The summation over each intensity scaled, block-specific PSF results in an image featuring anisoplanatic distortions and seeing effects attributable to imaging through turbulence over horizontal paths.

The remainder of this paper is organized as follows. In section 2.2 and 2.3 the theoretical framework used to justify the block-based approach is developed. In section 2.4 the necessity of incorporating multiple phase screens in order to properly simulate the turbulence volume along the imaging path is demonstrated. In section 2.5 the seeing effects present in this implementation are compared to theory; the presence of anisoplanatic effects is also verified. Using this method I have developed a set of 1000 images spanning three turbulence conditions, the generation of this data set is described in section 2.6. The Mean Squared Error (MSE) statistics in terms of per-pixel error in intensity for each image frame when compared to a diffraction-limited image are also examined in this section. Conclusions and suggestions for future work are provided in Section 2.7.

2.2 Theory

In this paper the problem of interest is the simulation of image formation under anisoplanatic conditions. The approach taken here is to model the anisoplantic imaging problem by dividing the object into regions small enough that isoplanatic conditions hold. The general form for the noise-free image formed under anisoplanatic conditions is

$$i(x_i, y_i) = \iint o(x_o, y_o) s(x_i, y_i, x_o, y_o, t) dx_o dy_o \tag{2.1}$$

where $o(x_o, y_o)$ is the object irradiance distribution in the object plane, $i(x_i, y_i)$ is the image formed by a monochromatic, incoherent imaging system located at a distance, L, from the object plane. The combined effect of the imaging system and the atmosphere is defined by a point spread function (PSF), $s(x_i, y_i, x_o, y_o, t)$, which is seen to be a function of location in the object and is time-varying.

Imaging under isoplanatic conditions can be considered as a special case of the general equation described above. The image formed in this case is convolution of the shift-invariant PSF with the object intensity distribution.

$$i(x_i, y_i) = \iint o(x_o, y_o) s(x_i - x_o, y_i - y_o, t) dx_o dy_o \tag{2.2}$$

For the horizontal imaging case this condition holds if the angular extent of the object at the imaging system is less than the isoplanatic angle defined for the horizontal case as[23]

$$\theta_0 = \left[2.91 k^2 \int_0^L C_n^2(z) z^{\frac{5}{3}} dz \right]^{-\frac{3}{5}} \tag{2.3}$$

In this expression, k, is the wavenumber and $C_n^2(z)$ is turbulence strength along the imaging path.

In this model the object is carved into a set of M by N blocks such that the angular extent of each block as viewed from the imaging system is less than the isoplanatic angle, θ_o, of the atmosphere along the imaging path. As a practical matter, while the isoplanatic angle may

serve as an effective upper bound on the size of each region, the region can be no smaller than the diffraction-limited angular sample rate of the imaging system $\Delta\theta_{x,y} = \lambda/2D$ where D is the diameter of the imaging system and λ is the imaging wavelength. Given this limit, even in the absence of turbulence effects, it would not be useful to reduce the size of each block in the object plane to less than $\Delta x_o, \Delta y_o = \Delta\theta_{x,y} L$. If this block size is used to partition the object, the center of each block with index value of $m = \{1,2,....M\}$, $n = \{1,2,....N\}$ will be located at $o(m\Delta x_o, n\Delta y_o)$.

Provided that angular extent of each region in this model is less than or equal to the the angular diffraction-limit the continuous object intensity distribution in Eq. 2.1 can be replaced by a discretely sampled image, $\hat{o}(m,n)$, such that

$$\hat{o}(m,n) = \iint o(x,y)\delta(m\Delta x_o, n\Delta y_o)dxdy \tag{2.4}$$

and because of the previous isoplanatic assumption the image formed under this model is equivalent to the summation of a series PSFs, $s_{m,n}(x_i, y_i, t)$,unique to each block m,n and weighted by $\hat{o}(m,n)$ allowing Eq. 2.1 to be rewritten as

$$i(x,y) = \sum_{m=1}^{M}\sum_{n=1}^{N} \hat{o}(m,n)s_{m,n}(x_i, y_i, t) \tag{2.5}$$

This result provides the basis for the development of the horizontal imaging simulation model. Details regarding the implementation of the simulation are provided in the next

section.

2.3 Generation of Block Specific PSFs

The method described in the previous section requires the generation of a single PSFs for every block or isoplanatic region in the object. In the phase screen methods used for simulation of imaging under isoplanatic conditions, a series of phase perturbations are applied to an unaltered, uniform amplitude field distribution across the aperture of an imaging system. The PSF may be derived in this case by taking the inverse Fourier transform of the perturbed field. If the phase distortions have the proper spatial statistics, the resulting PSF simulates the effects of atmospheric turbulence on imaging. For the more general case used in this paper the phase distortions and derived PSFs must display additional properties. Like the isoplanatic case, the power spectrum of the phase fluctuations must conform to the Kolmogorov turbulence model. In addition, for anisoplanatism to be expressed the PSFs for adjacent blocks must be correlated and the degree of correlation must decrease as the separation between them increases.

The approach used in this model uses N Kolmogorov phase screens to represent the turbulence volume. Using multiple screens builds in flexibility for future work, allowing the turbulence conditions to vary over the imaging path. Distributing the screens along the imaging path, rather than at a single location also ensures that both seeing and anisoplanatic

effects are accurately represented. Screens are arranged with uniform spacing such that the separation is $z_n = nL/N$ with $n = \{0, 1, 2...N-1\}$ so that the $n = 0$ screen is placed at the aperture and the final screen is placed $\Delta z = L/N$ from the object plane.

In order to generate screens with the correct spatial statistics, the turbulence strength and physical side length of the screens is required. Under isoplanatic conditions, the side-length is taken to be the projection of the aperture through the turbulence volume and is the same for each screen. In this model of the horizontal imaging problem the turbulence volume is represented as the projection of the aperture to the extent of the object, where the object is modeled as a series of blocks such the object has side length $l_o = M\Delta x_o = N\Delta y_o$. Each phase screen is modeled as a plane that intersects this volume at z_n parallel to the object plane. The side length of each screen used to generate the phase screen is

$$l_n = D + n\left(\frac{l_o - D}{L}\right)\Delta z \tag{2.6}$$

Accounting for spherical wave propagation in the model, the turbulence strength defined for each screen in terms of the Fried parameter, r_0, is defined by [18]

$$r_{0n} = 0.185\left[\frac{4\pi^2}{k^2 C_n^2(\frac{L-z_n}{L})\Delta z}\right]^{\frac{3}{5}} \tag{2.7}$$

The block-specific PSFs are generated by finding the region of each turbulence screen “seen" by each object block as it propagates geometrically toward the aperture. This region

is identified by forming a pencil ray between the center of the object block $o(m\Delta x_0, n\Delta y_o)$ and the origin of the optical axis located at the center of the imaging system aperture. Given an image of size $samples_i \times samples_i$, if each phase screen is generated such that it contains

$$samples_n = \frac{L}{\Delta z(N-n)} samples_i \tag{2.8}$$

a region of equal size and sampling to the aperture may be extracted from the turbulence screen without resorting to interpolation. To extract the region, the sample nearest to the intersection between the pencil ray and the plane of the screen is found. The surrounding $samples_i/2-1$ pixels are then extracted and combined, without interpolation, with the regions from the remaining screens, The block-specific PSFs are then derived from the perturbation of the unaltered field distribution using the traditional method [18]. The geometry relevant to the PSF generation process is summarized visually in Fig.2.1. The phase fluctuations in each screen are constrained as a function of separation by the turbulence strength specified when the screens are generated. As a consequence, for small block sizes adjacent PSFs should be highly correlated and separated blocks less so. It also follows (Eq. 2.7) that contributions to small scale fluctuations will be constrained to phase screens nearer to the aperture.

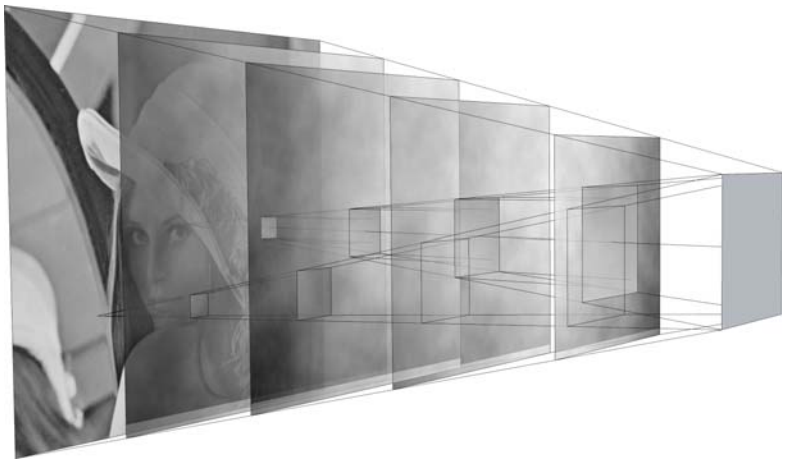

Figure 2.1: Visualization of the simulation geometry used to develop the block-specific PSF. Note that the size of each phase screen increases from the aperture on the right toward the object on the left

2.4 Representation of the Turbulence Volume As Discrete Phase Screens

Most models for near-ground turbulence assume a single turbulence strength, C_n^2, along constant-height, horizontal imaging paths [14]. The assumption of a constant value of C_n^2 allows for the turbulence volume to be modeled as a single phase screen under isoplanatic conditions. Considering the interest here in expressing anisoplanatic effects, it is useful to utilize multiple screens to properly express both seeing effects and anisoplanatism in the simulation. Using two extreme conditions, it is possible to make a heuristic argument to support this requirement. First, referring to Fig.2.1, consider first the case of a single phase screen placed across the imaging aperture. Under this condition, seeing effects are

reproduced exactly, but the entire field of view is within the isoplanatic angle of the imaging system. In the other extreme case a phase screen is placed directly at the object. Severe anisoplanatism will result but seeing effects, attributable to small scale fluctuations near the aperture, will not be present.

How may screens are necessary in this context is unclear. A general requirement for simulations relying on the split-step method is that the portion of the turbulence volume represented by a each phase screen must account for no more than 10% of the total scintillation along the imaging path [24],[16]. Though scintillation effects are ignored in this implementation, a minimum of four phase screens is prescribed under this criteria for $C_n^2 = 10^{-14}\mathrm{m}^{-2/3}$ and $L = 1000\mathrm{m}$. Similar criteria may be developed based on scale analysis considering the predicted turbulence outer scale or the atmospheric coherence length. These criteria result in a maximum number of screens which is generally quite large, on the order of a few hundred. Understanding that increasing the number of phase screens also increases computational requirements it is useful to understand how few screens can be used without sacrificing accuracy in the model.

To begin, consider the simple case of a single phase screen placed at an arbitrary position along the imaging path. Starting with Eq. 2.3 this condition can be approximated as

$$\theta_0^1 = \left[2.91 k^2 C_n^2 \int_0^L \frac{5}{3} \delta(z - z_i) dz \right]^{-\frac{3}{5}} \tag{2.9}$$

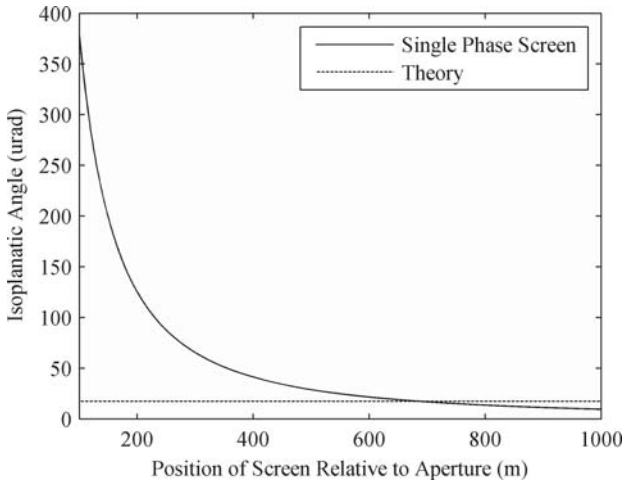

Figure 2.2: Predicted isoplanatic angle (solid) resulting from using a single phase screen to represent the turbulence volume as the screen is moved along a 1000m imaging path with the imaging system located at 0m. A 0.1m aperture is used and C_n^2 is 10^{-14} $\mathrm{m}^{-2/3}$. Note that the single screen is less than the theoretical value (dashed) for distances greater than about 700m. Although not shown in this figure values become asymptotic as the screen location near the aperture or the object

where the superscript in Eq. 2.9 indicates the use of a single phase screen to represent the turbulence volume. Numerical evaluation of this expression (Fig.2.2) produces an interesting, though not unexpected, result. For the conditions evaluated, the predicted isoplanatic angle is $\theta_0 = 17.7\mu$rad using the continuous theoretical model given in Eq. 2.3. Using the single-screen discrete model in Eq. 2.9 with a screen at the midpoint the predicted isoplanatic angle is $\theta_0^1 = 28.8\mu$rad a severe underestimate of this quantity. Inspecting Fig.2.2 it is also clear that the isoplanatic angle can be reduced by placing the screen closer to the object. In fact, the theoretical value may be duplicated by placing the screen at about 700 m for the 1000 m path length evaluated in this case. However, as noted earlier, moving the screen closer to the object reducing the prevalence seeing effects.

Table 2.1
Simulation turbulence parameters and derived values

Condition	C_n^2 ($m^{-\frac{2}{3}}$)	r_0 (cm)	$\frac{D}{r_0}$	θ_0 (μrad)	θ_o (pixels)
low	2.25×10^{-14}	3.45	3	10.8	4
moderate	3.25×10^{-14}	2.47	4	7.75	3
severe	5.25×10^{-14}	2.02	5	6.33	2

The expression for the isoplanatic angle resulting from using a single screen can be generalized for a model containing N uniformly spaced phase screens resulting in

$$\theta_0^N = \left[2.91 k^2 C_n^2 \sum_{n=1}^{n=N} \int_{(n-1)\frac{L}{N}}^{\frac{nL}{N}} \left(\frac{L}{N} \right)^{(\frac{5}{3})} dz \right]^{-\frac{3}{5}} \tag{2.10}$$

Numerical evaluation of Eq. 2.10 indicates that the expression converges toward the theoretical value in Eq. 2.3 as the number of uniformly spaced screens used increases (Fig.2.3). In addition, is is also possible to evaluate how well each configuration approximates the isoplanatic conditions predicted by theory. Using five screens results in an error in the resulting isoplanatic angle which is on the order of the diffraction limit for the conditions considered here while minimizing the computation resources needed for simulation. This value is also exceeds the four screens specified for split-step modeling based on the maximum scintillation criteria.

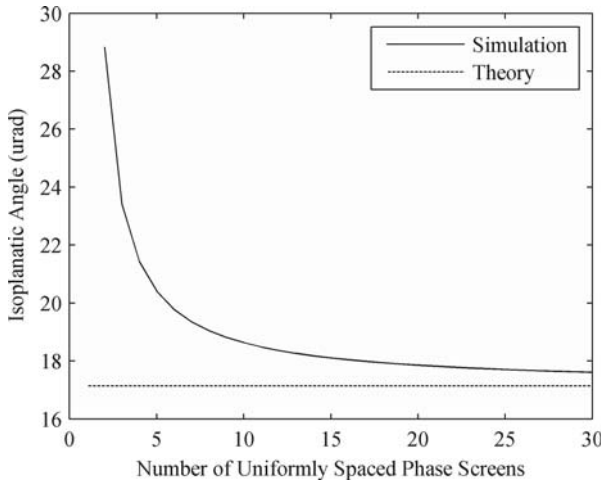

Figure 2.3: Isoplanatic angle resulting in approximating the continuous turbulence volume by a series of uniformly spaced, discrete phase screens. In this figure, $D = 0.1$m, $C_n^2 = 10^{-14}\text{m}^{-2/3}$, and $L = 1000$m.

2.5 Model Validation

The stated goal of developing this simulation method is the quantitative evaluation of image reconstruction techniques in the presence of turbulence featuring anisoplanatic distortions. Statistically rigorous, quantitative evaluation of these methods requires large data sets spanning a range of turbulence conditions. The choice was made to generate 1000 image frames over each of three turbulence conditions in the range of $C_n^2 = 10^{-14}$ m$^{-2/3}$ over a 1000m horizontal path using a 0.1m aperture imaging system. Three conditions, summarized in Table 2.1, were identified as producing, low, moderated and severe image degradation for this imaging system and path length. Corresponding values for the seeing parameter, r_0, and the isoplanatic angle, θ_0 are also provided in Table 2.1. In addition, values of D/r_0 and the isoplanatic angle in terms of image pixels are included for reference.

Having identified a range of turbulence conditions over which to generate a data set, a prudent next step is the validation of the model over these conditions. Validation of seeing effects is accomplished by comparing the long exposure PSFs produced for a single block to established theory. The theoretical long exposure PSF may be found by inverse Fourier transform of the ensemble average transfer function of the atmosphere is given here as [25]

$$H_{LE}(u,v) = \exp\{-57.4C_n^2 L f_{len}^{\frac{5}{3}} \lambda^{-\frac{1}{3}}(u^2+v^2)^{\frac{5}{6}}\} \tag{2.11}$$

where f_{len} is the imaging system focal length. The corresponding response of in the simulation method is found by averaging multiple frames when a single pixel, approximating a point source, is provided as an input. In Fig.2.4 the average of 500 of these frames is shown to match the theoretical values almost exactly over the span of turbulence conditions considered.

The presence of anisoplanatism effects in the simulation model may be verified using a similar procedure. Fig. 2.5 shows a set of outputs from the simulation model when a pincushion image is provided as an input. Sources in the image were spaced 30 pixels apart to prevent overlap and allow for visual verification of anisoplanatic effects over the image frame. In each of the images provided, one for each turbulence case, the distortion affecting each source clearly differs between sources and over the image frame. Quantifying the onset of anisoplanatic effects is realized by correlating PSFs as a function of separation in the image frame. The peak, normalized correlation coefficient as a function of separation

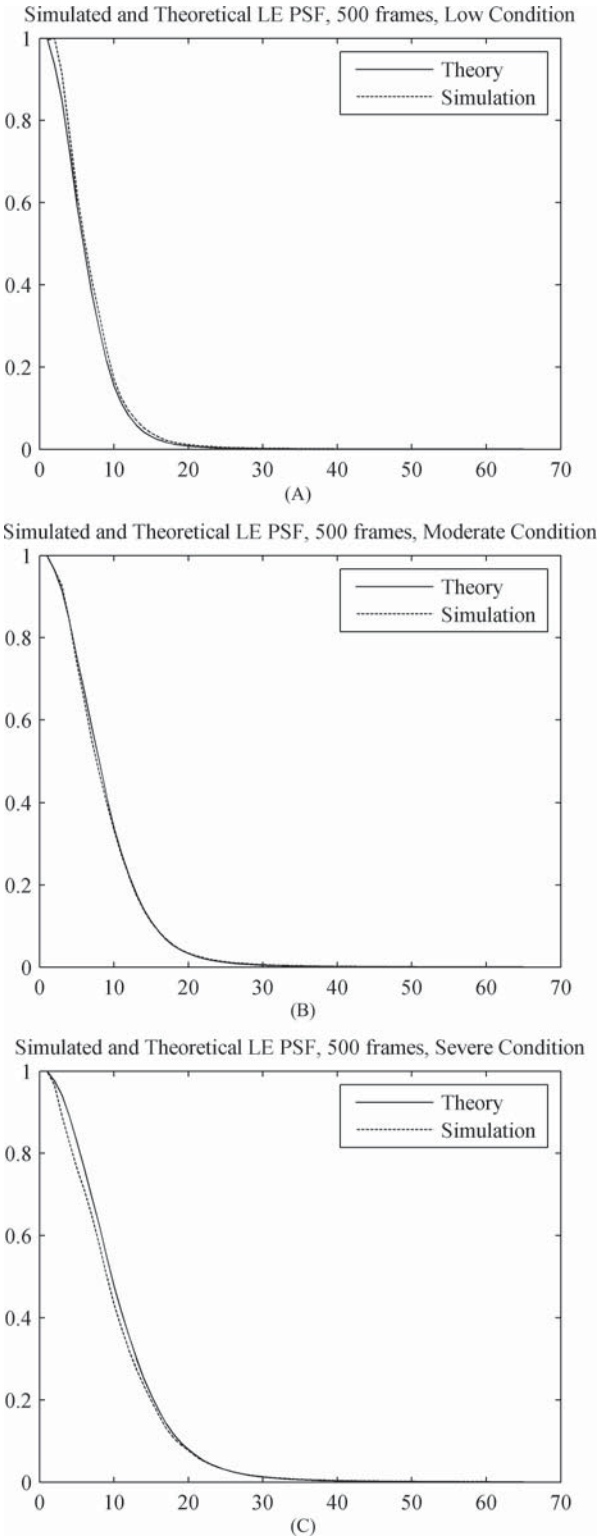

Figure 2.4: Predicted and Simulated, Radially Averaged, Long-Exposure PSFs for (A) Low, (B) Moderate, (C) Severe turbulence cases. Simulated PSFs are generated using 500 frames

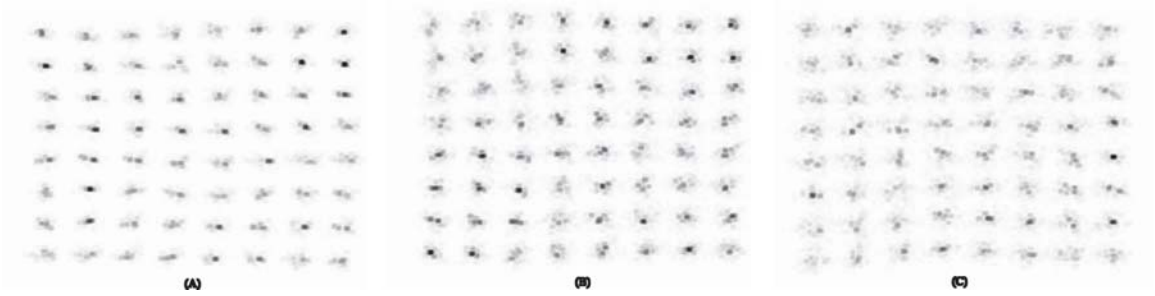

Figure 2.5: Point sources on 30 pixel spacing demonstrating anisoplanatism over a single image frame in simulator output for (A) Low, (B) Moderate, and (C) Severe turbulence conditions.

for the three turbulence conditions examined can be found in Fig. 2.6 . For each value in this figure a PSF was generated for the center location of the image and also at the indicated distance in pixels along each image axis in both directions. The value recorded represents the average of these four correlations over 100 instances. A consistent decrease in correlation is observed as separation and turbulence strength increases indicating the presence of anisoplanatic effects even at small angular separations in the image. Evaluation at the isoplanatic angles predicted by theory Eq. 2.3 for each case (Table 2.1) yields a correlation coefficient near 0.97 for each of the conditions examined.

2.6 The Horizontal Imaging Data Set

Following validation of the model, 1000 image frames were generated for each of the turbulence conditions in Table 2.1 using the "Lena" [26] image as the common source object for the data set. The Lena image features a human face, significant dynamic

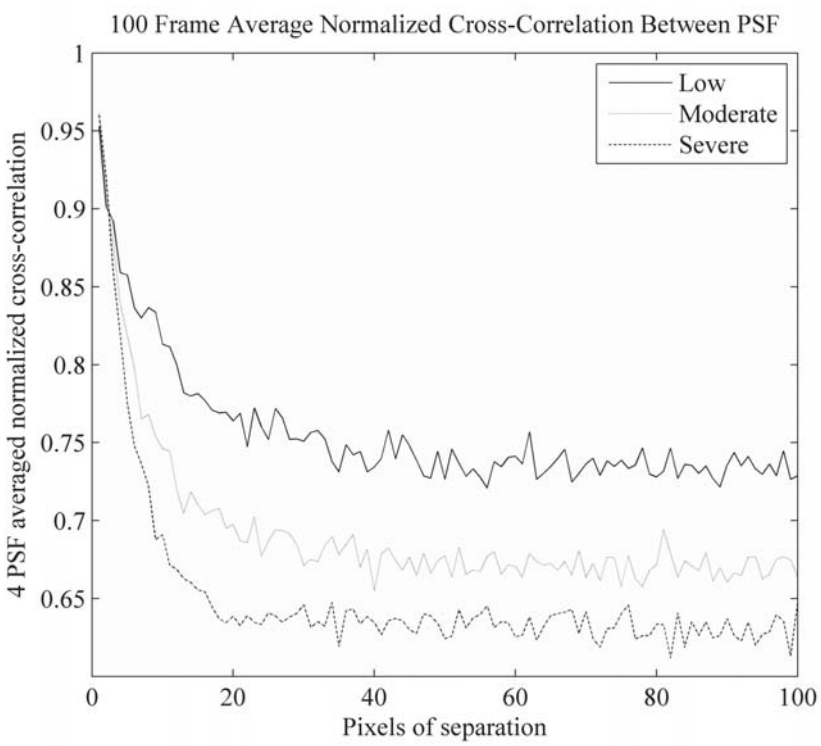

Figure 2.6: Average, peak, normalized cross-correlation between PSFs as a function of separation in image pixels. Each data point represents the average correlation between four PSFs along each axis and the PSF generated for the center pixel averaged over 100 independent turbulence volume realizations

range and an abundance of high-frequency spatial content; all important visual cues for subjectively evaluating image quality. Generating each frame in MATLAB® required approximately 40 minutes on a Intel 2.1 GHz Xeon processor and approximately 90 days of computer time were required to generate the data set. A turbulence-free, diffraction-limited image and an example image from each of the data sets is provided in Fig. 2.7; note that both atmospheric seeing and anisoplanatic effects are evident in the simulation output.

In addition to a data set, an objective metric is also needed to properly quantify image

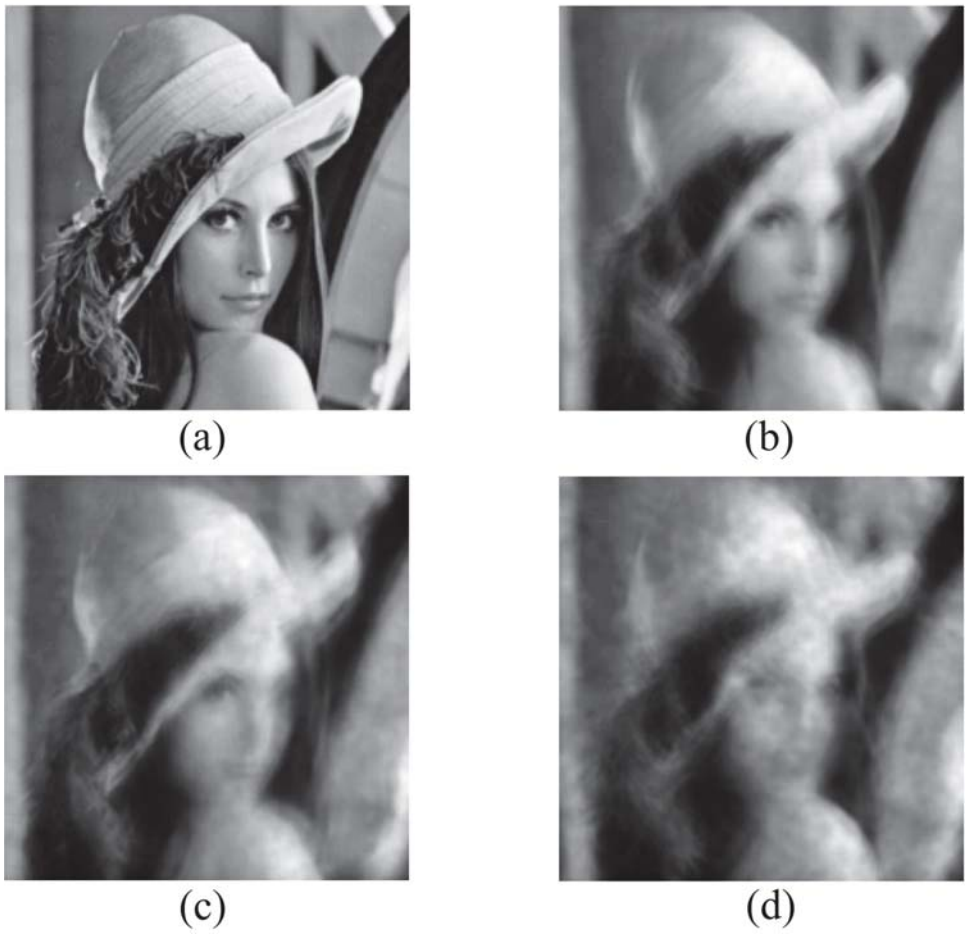

Figure 2.7: Simulator output for the (A) Diffraction-Limited, (B) Low, (C) Moderate, (D) Severe turbulence conditions listed in Table 2.2

reconstruction performance; the MSE is used here though other metrics may suffice. To provide a baseline for understanding the performance of these methods the MSE statistics were collected for each data set and analyzed. The MSE in intensity value per pixel was calculated for each frame by first centering the frame on the diffraction-limited reference

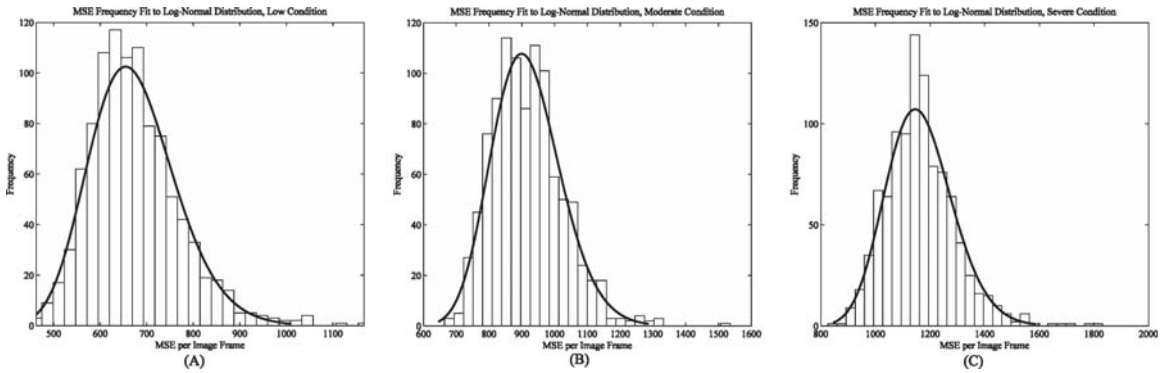

Figure 2.8: MSE count frequency and associated log-normal fit for the Low(A), Moderate(B), and Severe(C) data sets.

image in Fig. 2.7. The MSE for each image frame is then calculated as

$$MSE_f = \frac{1}{MN} \sum_{m=1}^{M} \sum_{n=1}^{N} |i(m,n) - o(m,n)|^2 \tag{2.12}$$

Fig. 2.8 features the distribution of MSE per frame(Eq. 2.12) for each data set. A log-normal distribution has also been fitted to each distribution having been found to provide the best fit to the errors frequency in each distribution [27]. It is oberved that the average MSE in each dataset increases from 673 counts for the low condition to 1165 counts for the severe condition approximately linearly as a function of turbulence strength in terms of C_n^2. The variation about the mean is observed to decrease slightly as turbulence strength increases from 13.9% to 10.5%. A summary of the MSE statistics for each data set can be found in Table 2.2.

Table 2.2
Log-Normal Parameters for MSE Statistics

	r_0 (cm)	μ	σ^2
Low	3.45	673	8755
Moderate	2.47	917	11168
Severe	2.02	1165	14961

2.7 Conclusion

A simulation model that accurately reproduces seeing and anisoplanatic effects observed in images acquired over horizontal path has been developed. This model has been used to generate a data set of 3000 turbulence-corrupted images based on a pristine input image. Using this data set, the performance and robustness of image reconstruction techniques applied to the horizontal imaging problem may be objectively evaluated. A baseline analysis of the image degradation in terms of the MSE in intensity value per pixel was also undertaken for each data set. This analysis indicates that the distribution of errors in each data set is log-normal with a mean value that increases with turbulence strength. To be considered robust, the mean and variance in residual MSE present in reconstructions derived from this data set must be lower than this established baseline.

Images in this data set were generated using five phase screens placed uniformly with the aim of duplicating conditions found over horizontal or slightly slanted paths. It was possible, using five phase screens, to validate seeing effects in the model to theory. It

remains possible that anisoplanatic effects may still be slightly under-expressed. Using more sophisticated workstations and incorporating additional phase screens the accuracy of the model may be improved. Though not explored here, the distributed phase screen model also allows for differing turbulence profiles to be explored. For example, by increasing the relative turbulence strength of screens nearer the object it may be possible to simulate severe slant path conditions. More specialized topographic scenarios (i.e. partially over water paths) may be simulated in a similar manner by manipulating the turbulence strength and spacing between screens. Of course, in all of the cases, including the one presented here, some attempt at validation against field conditions is also warranted.

Chapter 3

Robustness of Speckle Imaging Techniques Applied to Horizontal Imaging Scenarios

[1]

[1]The material contained in this chapter was previously published in the journal Optical Engineering published online on August 3, 2012 [2] and is scheduled to appear in print in the August 2012 issue of the journal. See Appendix C for documentation of permission to republish this material.

3.1 Introduction

The turbulent atmosphere near the Earth's surface has a deleterious effect on the performance of horizontally-tasked imagers which must operate at ranges of a few hundred meters out to several kilometers. The desire to improve the quality of imagery provided by these systems has motivated research into methods for mitigating turbulence effects encountered over horizontal paths. A significant number of these methods have their origins in the imaging of space objects where the problem has been the subject of active research for over 50 years. Due to differences in the physics of the underlying problem, some of these methods are better suited to horizontal imaging than others. Specifically, in the imaging of space objects, it is often convenient to assume that atmospheric turbulence is concentrated in a thin layer directly above the imaging aperture. Moreover, objects of interest are distant, spanning at most a few arc seconds. As a result of these conditions, the effect of turbulence is constant over the angle subtended by the object, a condition referred to as isoplanatic. In contrast, objects of interest in horizontal imaging scenarios generally span much larger angles at more modest distances. As a consequence, the isoplanatic assumption no longer holds. Indeed, in many horizontal imaging scenarios the isoplanatic angle may be on the order to the diffraction limit of the imaging system.

Horizontal imagers are also likely to have significantly different operational requirements. For example, they are generally operated by novice users and may be included in

man-portable systems. In both cases, it is necessary that the system perform effectively over a wide range of conditions without requiring user interaction. These systems are also likely to have modest imaging apertures compared to those used in observatory telescopes. In most horizontal imaging scenarios, reconstructions must also be provided to the user in real-time, implying that a certain level of computational efficiency is required. For portable systems, weight, and therefore power consumption is of concern. Consideration of these requirements leads to the conclusion that some sort of embedded image processing system is necessary to achieve operational goals. Bearing in mind the expense involved in developing embedded systems, most engineering organizations would be reluctant to expend the resources necessary without first fully vetting the underlying image processing algorithm. Such efforts begin by finding a design solution most likely to meet the requirements and then continue by evaluating the design over the expected variation in operational parameters. The set of these parameter variations, including variations due to use by novice users, are identified as the system noise parameters. Designs that possess a certain level of immunity to the variation in these noise parameters are considered to be robust.

It is interesting then, to understand which image post-processing techniques can be shown to robust considering these requirements. A number of image post-processing techniques have been developed specifically for use in horizontal imaging applications. For example, Fraser [28] has suggested a method by which tip-tilt distortions are removed first globally, and in successively smaller sub-regions, finally reaching the level of a single pixel; residual

image blur is compensated by traditional deconvolution techniques. Carhart and Vorontsov [20], [29] have suggested a technique based on the idea of lucky frame selection whereby the highest quality subregions over a series of short exposure image frames are combined to generate a single high quality image. The idea of applying speckle imaging techniques to horizontal imaging scenarios was first suggested by Carrano [30]. The performance acheived by speckle imaging, in particular, was promising enough that an embedded speckle imaging system has been developed [31]. However, the degree to which any of these methods maintain their performance over variation in operational conditions is still largely unknown. In Chapter 2 a horizontal imaging simulation model [1] was developed and used to develop a data set of 1000 images for each of three turbulence conditions based on the "Lena" test image [26]. Utilizing this data set, the quantitative evaluation of performance of each of these methods may be examined over the variation in their relevant noise parameters. For speckle-imagers these parameters include design parameters such as the number of input frames and the number of estimates of the object phase. Parameters that are estimated or tuned by the user in the pseudo-Weiner filter are also treated as noise parameters in this work.

In this work, the robustness of speckle imaging techniques applied to horizontal imaging scenarios is evaluated. Beginning in section 3.2, the horizontal imaging problem is discussed in a detail. A requisite review of speckle imaging and the factors important in reconstruction performance using speckle imagers is provided in section 3.3. This analysis continues by defining robustness as it applies to horizontal imagers in section 3.4,

before providing results in section 3.5. The analysis indicate that, for daylight, horizontal imaging scenarios speckle imaging performance is stable when more than 15 input frames are used in each estimate along with 4 estimates of the object phase. Similarly, if the user is able to provide a rough estimate of the seeing conditions along the path reconstructions near the performance limit of the estimator may be obtained. A complete review of the conclusions and recommendations resulting from this work are provided in section 3.6. It is assumed that the target object does not significantly affect speckle imaging performance as long as that target is a natural scene. To check this assumption these analyses are repeated on a second simulated image set featuring the "Boats" reference image [32] and the same simulation parameters as the "Lena" set. No significant performance differences were observed between the two analyses. Summarized results of this second analysis and a descriptions of the second data set are included as appendices to this dissertation for completeness.

3.2 Horizontal Imaging

Horizontal imaging, as described here, can be considered a special case of the general problem of imaging through turbulence. In general, the effect of turbulence is to reduce the resolution available to imaging systems. It is often useful to describe the resolution available to a turbulence-limited imaging system in terms of the equivalent diffraction-limited radius, or atmospheric coherence radius, r_0, defined by Fried [33],[18]

as

$$r_0 = \left[0.4217 k^2 \int_0^L \left(\frac{L-z}{L} \right) C_n^2(z) dz \right]^{-\frac{3}{5}} \tag{3.1}$$

where λ is the mean imaging wavelength, L is the imaging path length, $k = 2\pi/\lambda$ is the wavenumber, and C_n^2 is turbulence strength parameter, provided as a function of distance, z, along the imaging path. Note that the expression in Eq. 3.1 is valid for spherical wave propagation, an appropriate assumption for the horizontal imaging conditions. It is also common to assume that the turbulence strength, C_n^2, is constant over the imaging path for fixed heights above the ground. This second assumption allows Eq. 3.1 to be written as

$$r_0 = (0.16 C_n^2 k^2 L)^{-\frac{3}{5}} \tag{3.2}$$

This quantity may be used to define the effective resolution available to an imaging system when the exposure time is much longer than the coherence time of turbulence in atmosphere. Using a linear system framework the available image is expressed as the convolution of an object irradiance distribution and a Point Spread Function (PSF) which includes the effects of both the imaging system and turbulence effects. Analysis in this case is usually performed with Fourier transformed quantities allowing the Fourier spectrum of the resulting image, $I(\vec{f})$ to be expressed as

$$I(\vec{f}) = H_{LE}(\vec{f}) O(\vec{f}) \tag{3.3}$$

where $O(\vec{f})$ is complex frequency spectrum of the object irradiance and [18]

$$H_{LE}(\vec{f}) = \exp\left\{\frac{1}{2} - 6.88\left(\frac{\lambda D|\vec{f}|}{r_0}\right)^{\frac{5}{3}}\right\} \tag{3.4}$$

is the long exposure atmospheric Optical Transfer Function (OTF) and D is the aperture diameter of the imaging system.

A significant limitation of Eq. 3.4 is that is does not apply to imaging over short time-scales. A similar expression for short-exposure [33] imaging is available but it does not include bulk tip and tilt effects. These tip-tilt distortions are only uniform over an area smaller than the isoplanatic angle, defined here as

$$\theta_0 = \left[2.91k^2 \int_0^L C_n^2(z) z^{5/3} dz\right]^{-\frac{3}{5}} \tag{3.5}$$

Objects spanning angles greater than θ_0 are subject to independent tip and tilt distortions, in addition to higher order distortions, and are not shift-invariant. The presence of these anisoplanatic distortions is a defining trait of imagery acquired over horizontal paths.

In addition to the assumptions regarding the turbulence characteristics over horizontal paths, the definition of horizontal imaging used here is further limited to include the following characteristics. First, it is assumed image acquisition occurs during daylight such that image detection can be approximated with Gaussian statistics and that Poisson statistics associated with photon-limited imaging can be safely ignored. As a result, for

the high Signal to Noise Ratio (SNR) scenarios of interest here, the only relevant noise characteristics of concern are due to read noise from the imaging CCD. It is also assumed that acquisition takes place over horizontal or slight slant paths on the order of a few hundred meters up to a few kilometers. Turbulence strengths over these paths can assumed to be constant and magnitude of C_n^2 is limited such that scintillation effects are may be ignored.

3.3 Speckle Imaging

In speckle imaging, the amplitude and phase of the object Fourier transform are estimated in separate steps using the ensemble statistics of each quantity over the provided input frames. A single reconstructed image frame is developed via inverse Fourier transform of the combined estimates. The amplitude estimate is obtained by inverse filtering the average Power Spectral Density (PSD) of each short exposure input frame using a Weiner filter

$$|\hat{O}(\vec{f})|^2 = \frac{\langle |I(\vec{f})|^2 \rangle}{|\hat{H}_{LE}(\vec{f})|^2 + \alpha} \tag{3.6}$$

where $\hat{H}_{LE}$ is the estimate of the long exposure Optical Transfer Function (OTF) of the atmosphere based on Eq. 3.4. In astronomical imaging scenarios the quantity, $\hat{H}_{LE}$, in Eq. 3.6 is measured by observation of a nearby natural or artificial point source such as a star. Such sources are not often found in horizontal imaging, requiring the turbulence strength

used in Eq. 3.4 be estimated based on time of day and imaging path length via Eq. 3.2. These estimates often lack accuracy, resulting in reduced reconstruction quality. Eq. 3.6 also includes a noise regularization parameter, α, which is generally tuned according to user preference.

Taken on its own, the amplitude estimate provided by Eq. 3.6 lacks the object phase information necessary to reconstruct an image. To estimate the object phase the object cross-spectrum [5] or bispectum [6] are employed. These quantities are defined as

$$C(\vec{f},\Delta\vec{f}) = I(\vec{f})I^*(\vec{f}+\Delta\vec{f}) \tag{3.7}$$

for the cross-spectrum, and

$$B(\vec{f},\Delta\vec{f}) = I(\vec{f})I(\Delta\vec{f})I^*(\vec{f}+\Delta\vec{f}) \tag{3.8}$$

for the bispectrum. In both quantities, $\Delta\vec{f}$ represents an incremental offset in frequency relative to $\vec{f}$. Phase is recovered using the Knox-Thompson technique by first substituting Eq. 3.3 into Eq. 3.7 and expanding result in terms of the amplitude and phase of each

quantity resulting in

$$C(\vec{f},\Delta\vec{f}) = \quad |O(\vec{f})||O^*(\vec{f})||H_{atm,n}(\vec{f})||H^*_{atm,n}(\vec{f}+\Delta\vec{f})| \times \exp\left\{ j\left[\phi_o(\vec{f}) - \phi_o(\vec{f}+\Delta\vec{f}) + \phi_{H,n}(\vec{f}) + \phi_{H,n}(\vec{f}+\Delta\vec{f})\right]\right\} \tag{3.9}$$

In Eq. 3.9, $H_{atm,n}$ is the, random, instantaneous atmospheric OTF, including imaging system effects degrading deterministic object spectrum $O(f)$ and $\phi_{H,n}(\vec{f})$ is the phase associated with this quantity. Taking the expectation of Eq. 3.9 over N image frames results in

$$\langle C(\vec{f},\Delta\vec{f})\rangle_N = \quad |O(\vec{f})||O^*(\vec{f})|\langle|H_{atm,n}(\vec{f})||H^*_{atm,n}(\vec{f}+\Delta\vec{f})|\rangle_N \times \exp\left\{ j\left[\phi_o(\vec{f}) - \phi_o(\vec{f}+\Delta\vec{f}) + \langle\phi_{H,n}(\vec{f}) + \phi_{H,n}(\vec{f}+\Delta\vec{f})\rangle_N\right]\right\} \tag{3.10}$$

Amplitude and phase contributions from the atmosphere in Eq. 3.10 are referred to the as the average atmospheric cross-spectrum transfer function. It can be shown, that this quantity is real and therefore $\left\langle \phi_H(\vec{f}) + \phi_H(\vec{f}+\Delta\vec{f})\right\rangle = 0$. Subsequently the object

phase is retained in the cross-spectrum and may be recovered recursively. Specifically, the phase at an unknown frequency, $\vec{f}' = \vec{f} + \Delta\vec{f}$, is found using the cross-spectrum or Knox-Thompson(KT) method as

$$\phi_o(\vec{f}') = \phi_o(\vec{f}) - \langle \phi_{KT}(\vec{f}, \Delta f) \rangle \tag{3.11}$$

A similar exercise may be undertaken using the bispectrum resulting in,

$$\phi_o(\vec{f}') = \phi_o(\vec{f}) + \phi_o(\Delta f) - \langle \phi_B(\vec{f}, \Delta f) \rangle \tag{3.12}$$

In both cases, phasor quantities are generally used to avoid modulo π ambiguities. Initializing the recursions in Eq. 3.11 and Eq. 3.12 requires an assumption be made regarding the object. The real-valued nature of images implies a zero phase value at DC, $|\vec{f}| = 0$ in both methods, this assumption alone is sufficient to begin recovery using the KT. For the bispectrum, it is also necessary to set the value adjacent to the origin, $|\Delta f = 1|$, to zero. This second assumption results in a loss of relative spatial information which is of little consequence in imaging space-based objects but complicates the reconstruction of extended scenes common to horizontal imaging. Upon further inspection of Eq. 3.11 and Eq. 3.12 it is also evident that if the desired object phase frequency, $\vec{f}' = \vec{f} + \Delta\vec{f}$, is fixed, there exist multiple independent values of $\vec{f}$ and $\Delta\vec{f}$ which satisfy the relationship. In practice, the estimate of the object phase at each spatial frequency in the object spectrum is derived using multiple combinations in the bispectrum or cross-spectrum phase. A number

estimators are available [10], [11], that can be used to obtain an optimum estimate for the object phase, though these approaches introduce significant computational complexity. The generalized approach taken uses only the average from a limited number of sub-planes, Δf, of the cross and bispectrum; this method can be described in a simplified form for the bispectrum

$$\phi_{ob}(\vec{f}') = \frac{1}{N_p} \sum_{\Delta\vec{f}=1}^{N_p} \left[\phi_o(\vec{f}' - \Delta\vec{f}) + \phi_o(\Delta\vec{f}) - \beta(\vec{f}' - \Delta\vec{f}, \Delta\vec{f}) \right] \tag{3.13}$$

and the cross spectrum as

$$\phi_{oc}(\vec{f}') = \frac{1}{N_p} \sum_{\Delta\vec{f}=1}^{N_p} \left[\phi_o(\vec{f}' - \Delta\vec{f}) - KT(\vec{f}' - \Delta\vec{f}, \Delta\vec{f}) \right] \tag{3.14}$$

The quantities $\beta(\vec{f}', \Delta f)$ and $KT(\vec{f}', \Delta\vec{f})$ in Eq. 3.13 and Eq. 3.14 are the unbiased estimators for the bispectrum [7], [18]

$$\begin{aligned} \beta(\vec{f}, \Delta\vec{f}) = \quad & I(\vec{f}) I(\Delta\vec{f}) I^*(\vec{f} + \Delta\vec{f}) - \\ & |I(\vec{f})|^2 - |I(\Delta\vec{f})|^2 - |I(\vec{f} + \Delta\vec{f})|^2 + 2K + 3P\sigma_n^2 \end{aligned} \tag{3.15}$$

and cross spectrum

$$KT(\vec{f},\Delta\vec{f}) = I(\vec{f})I^*(\vec{f}+\Delta\vec{f}) - I^*(\Delta\vec{f}) \tag{3.16}$$

In Eq. 3.15, K is the total number photo-events in real image frames, or for arbitrary units $K = |I(\vec{f}=0,0)|$; σ_n is the standard deviation of the additive noise present in image frames. Note that the SNR of the cross and bispectrum decreases as the magnitude of the offset frequency sub-plane, $\Delta\vec{f}$, increases [7]. So, it is not always the case that increasing N_p results in an improvement in image quality. The number of recursion paths, N_p in Eq. 3.13 and Eq. 3.14 is taken to be the number of phase estimates used for each reconstruction. As a design parameter, the number of phase estimates can affect both image quality and reconstruction time.

Because the bispectrum is shift-invariant it is favored over the KT for phase retrieval in most speckle imaging applications. Examining Eq. 3.7 and Eq. 3.8 it is also evident that the bispectrum is identical to the cross-spectrum apart from a frequency dependent scaling factor which provides for improved reconstruction performance at low light levels. The shift-invariance and weighting of the bispectrum provide a substantial advantage in photon-limited imaging cases. The scenarios of interest here are not photon-limited, and while it may appear that shift invariance would still be preferred it is irrelevant in the imaging of extended objects. For extended objects, the limited support condition is enforced artificially by zero padding the scene presented to the estimator. This scene must

be consistent between image frames imposing the requirement that images be registered prior to processing. Under these conditions I assert that the bispectrum and KT methods are essentially identical apart from the additional computations required to support the weighting in the bispectrum algorithm. I also note that reconstructions produced using the bispectrum method require a separate post-reconstruction registration step that adds to the overall computation burden. In this work, the KT method is examined along side the traditional bispectrum method used for speckle-imaging with the goal of proving the assertion of equivalence between the two methods.

3.4 Robustness

The goal in this work is to establish the robustness of speckle imagers in horizontal imaging applications. This goal is ambiguous due to the many definitions of robustness that exist throughout engineering literature. In this work, robustness is defined as immunity to the factors that cause variability in performance. These factors are further defined as both the range of conditions over which the estimator is expected to operate and the range of user controlled or free parameters. These are parameters that are either estimated or tuned by the user and may affect estimator performance. Also included in this definition is a certain stability of performance in the presence of noise in collected input frames.

Traditionally, the evaluation of robustness requires the use of a metric that can be directly

related to the SNR. In this work, the Mean Squared Error (MSE) in normalized intensity pixel values is used for this purpose. While not ideal as a metric of image quality, it is well established and straightforward to implement. The main drawback to the use of the MSE, or any SNR-based metric, is the requirement that a reference image be used in order to evaluate the quality of the reconstruction. This requirement, and the need to carefully control input conditions, strongly suggests that a simulation is necessary to perform this analysis.

In a Chapter 2, a simulation model was developed that produces images containing both anisoplanatic distortions and atmospheric blurring. To produce these images a reference image is sampled spatially at the object plane at a rate equal to the angular diffraction limit for the simulated imaging system. Using a geometric optics approach a ray is traced from a sample in the reference image, located at the object plane, to every pixel in the detector of the simulated imaging system. Turbulence effects are introduced via a series of random phase screens, with Kolmogorov spatial statistics, placed uniformly along the imaging path. Phase errors are accumulated along each ray and applied as a set of perturbations to the unperturbed aperture field distribution. This perturbed aperture distribution is used to develop a PSF that is specific to a single sample in the reference object and differs as a function of separation in the object plane.

In this model a PSF is developed for each sample in the reference image. Images are formed by summation over each PSF, weighted by the sampled intensity of the reference

image. New images are created by repeating the process with new phase screen instances. Using this technique a simulated data set of 3000 image frames was developed. The simulated data set spans three turbulence conditions in the range of $C_n^2 = 10^{-14}$ m$^{-2/3}$. Each frame simulates the image formed by a 0.1m aperture imaging system, with $\lambda = 700$ nm, observing a 0.75m object over a 1000 m path through a turbulence volume. For each turbulence condition 1000 image frames were generated using the "Lena" [26] image as the reference image. Intensity values in each simulated frame are normalized to values between 0 and 255 and each image is then registered against a diffraction-limited template using the peak normalized cross-correlation coefficient. The MSE in normalized intensity value per pixel, for each frame, i, with pixel locations, (m,n), compared to diffraction-limited template, o is found as

$$MSE_f = \frac{1}{MN} \sum_{m=1}^{M} \sum_{n=1}^{N} |i(m,n) - o(m,n)|^2 \tag{3.17}$$

A summary of the MSE statistics across the three turbulence conditions in the data set and a summary of the turbulence parameters is found in Table 3.1. In a previous work [1] the distribution of errors in terms of normalized intensity pixel values per frame over each data set were found to be distributed log-normally. The MSE statistics presented in Table 3.1 are the best fit parameters to a log-normal distribution. Example output frames from the simulation tool are provided in Fig. 3.1.

This baseline analysis of the simulated data establishes a criteria for the robustness of

Table 3.1
Simulation turbulence parameters and log-normal statistics used to develop the "Lena" data set. The terms "Low", "Moderate" and "Severe" are used as labels to identify the data sets and indicate the effect of integrated turbulence on imaging over the simulation path in the moderate turbulence regime.

Condition	C_n^2 ($m^{-\frac{2}{3}}$)	r_0 (cm)	θ_0 (μrad)	μ_{MSE}	σ_{MSE}
"Low"	2.25×10^{-14}	3.33	10.52	673	96
"Moderate"	3.75×10^{-14}	2.45	7.74	917	106
"Severe"	5.25×10^{-14}	2.02	6.38	1165	122

candidate estimators. To be considered a capable estimator the mean residual MSE of reconstructed image frames must be lower than that of the input data set. Further, the variance in the residual MSE across reconstruction frames must also be lower than the variance in the input data set. Obviously, smaller values for both quantities is evidence of a higher quality estimator. A parametric tuning of the design parameters associated with speckle imagers will allows the identification of a subset of parameters on which to optimize when designing and implementing systems based on these methods.

A number of parameters influence the reconstruction quality available to speckle imaging systems. One obvious parameter is the severity of the turbulence conditions during the observation time. The other parameters affecting image reconstruction quality are either fixed by the designer or tuned by the user. These parameters are: the number of input frames, the user estimate of C_n^2, the noise regularization parameter, α in Eq. 3.6, and the number of independent phase estimates per spatial frequency. The choice of the number of input frames, N_f, and object phase estimates, N_p, has a direct effect on the image

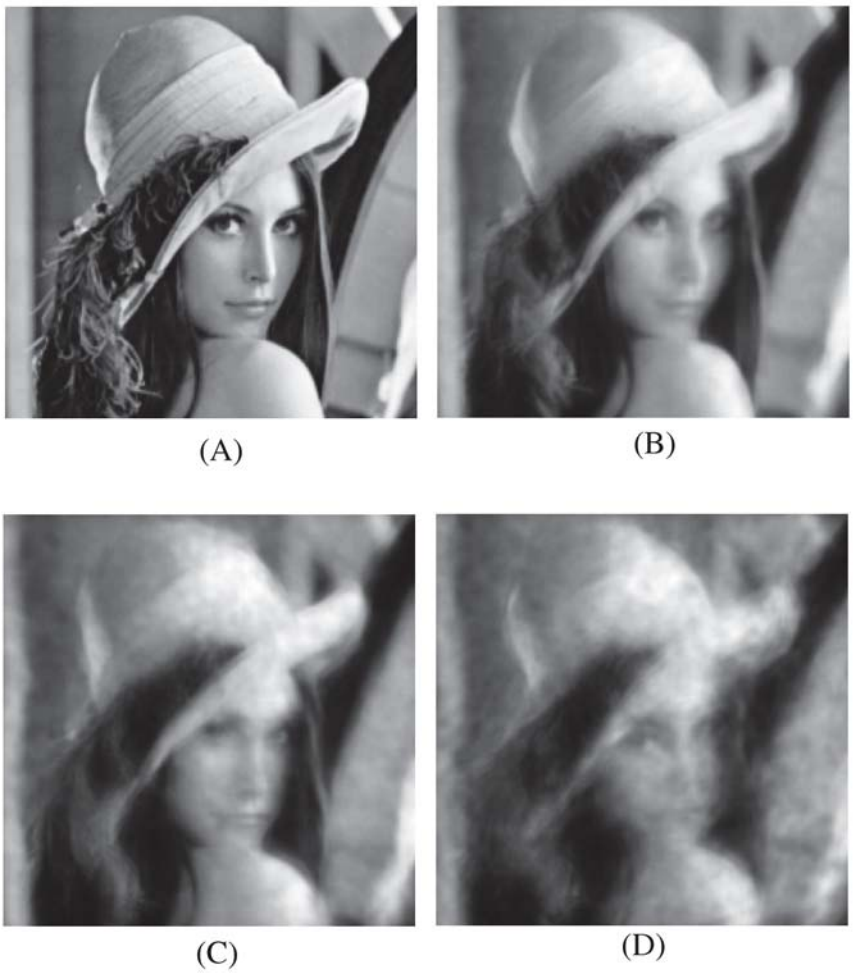

Figure 3.1: Example frames from the "Lena" simulated data set. Image frames in the panel are for (A) diffraction-limited, (B) "Low", (C) "Moderate", and (D) "Severe" conditions.

reconstruction time and is therefore of interest to the designer. Estimates for the two Weiner filter parameters are generally estimated or tuned by the user though the designer may still choose to restrict the range of values available to the user to ensure adequate reconstruction quality. Finally, the detection statistics for each pixel are assumed to be adequately modeled by non-zero mean Gaussian processes. However, at high frame rates the presence of additive noise attributable to imaging CCD electronics must be considered.

Each of these factors are accounted for in this analysis of the robustness of speckle imagers.

3.5 Results

3.5.1 Effect of variation in α on reconstruction performance

This analysis begins by examining the influence of the the value of the Weiner filter noise parameter, α in Eq. 3.6, on reconstruction performance. As mentioned previously, this value is traditionally tuned according to user preference and has no theoretical minimum value in the absence of additive noise. In the presence of noise, the optimum value of this parameter is theoretically related to the SNR of the input signal and independent of the distortion strength. In either case, it is of interest to understand the value of this parameter that results in the minimum MSE; especially when additive noise effects are considered. Based partially on experiment, a region of interest for this parameter was established over the range $\alpha = \{0.01...2.0\}$. Evaluation was undertaken for each of the three turbulence conditions, with the number of frames was fixed at $N_f = 50$ allowing for performance evaluation over $N = 20$ independent reconstructions. A default value of $N_p = 5$ phase estimates was used to estimate the phase at each frequency in the object spectrum. The value of C_n^2 used in the Weiner filter is set to the theoretical value used in the simulation model used to generate the data set. Results are displayed separately for

the three turbulence conditions in Fig. 3.2. An optimum value near $\alpha = 0.4$ was recorded for each turbulence condition and is used as a default value in the analysis of the other parameters explored in this work.

3.5.2 Effect of variation of α on reconstruction performance in the presence of additive noise

The noise parameter in Eq. 3.6 is theoretically dependent on SNR. Bearing in mind this dependence, the optimum value of α should vary as the level of additive noise in the image is increased. To explore this relationship, zero-mean additive Gaussian, $\sigma_n = \{1, 2, ..10\}$ was added to input frames and the value of α varied. The results of this analysis is presented in Fig. 3.3. Examination of Fig. 3.3 indicates that MSE as affected by variation in the Weiner filter noise parameter is at most a weak function of turbulence strength and saturates for high noise levels. The slight increases in MSE at $\alpha = 0.4$ and 1 can be attributed to slight misalignments in image registration at high noise levels. Optimum values, specific to the image set, were recorded and used when the evaluating the variation of the other parameters examined in this work. No significant change in the variance in residual MSE is observed regardless of the value of α or noise level.

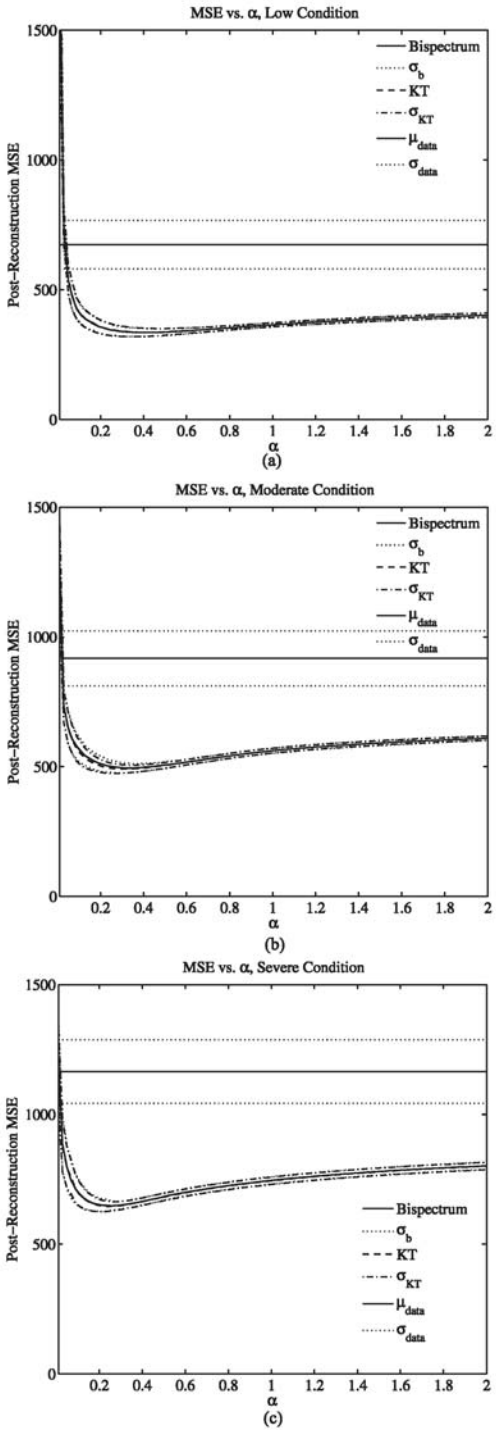

Figure 3.2: Evaluation of the effect on the post-reconstruction, residual MSE observed by varying α for the (a) "Low", (b) "Moderate", and (c) "Severe" turbulence conditions.

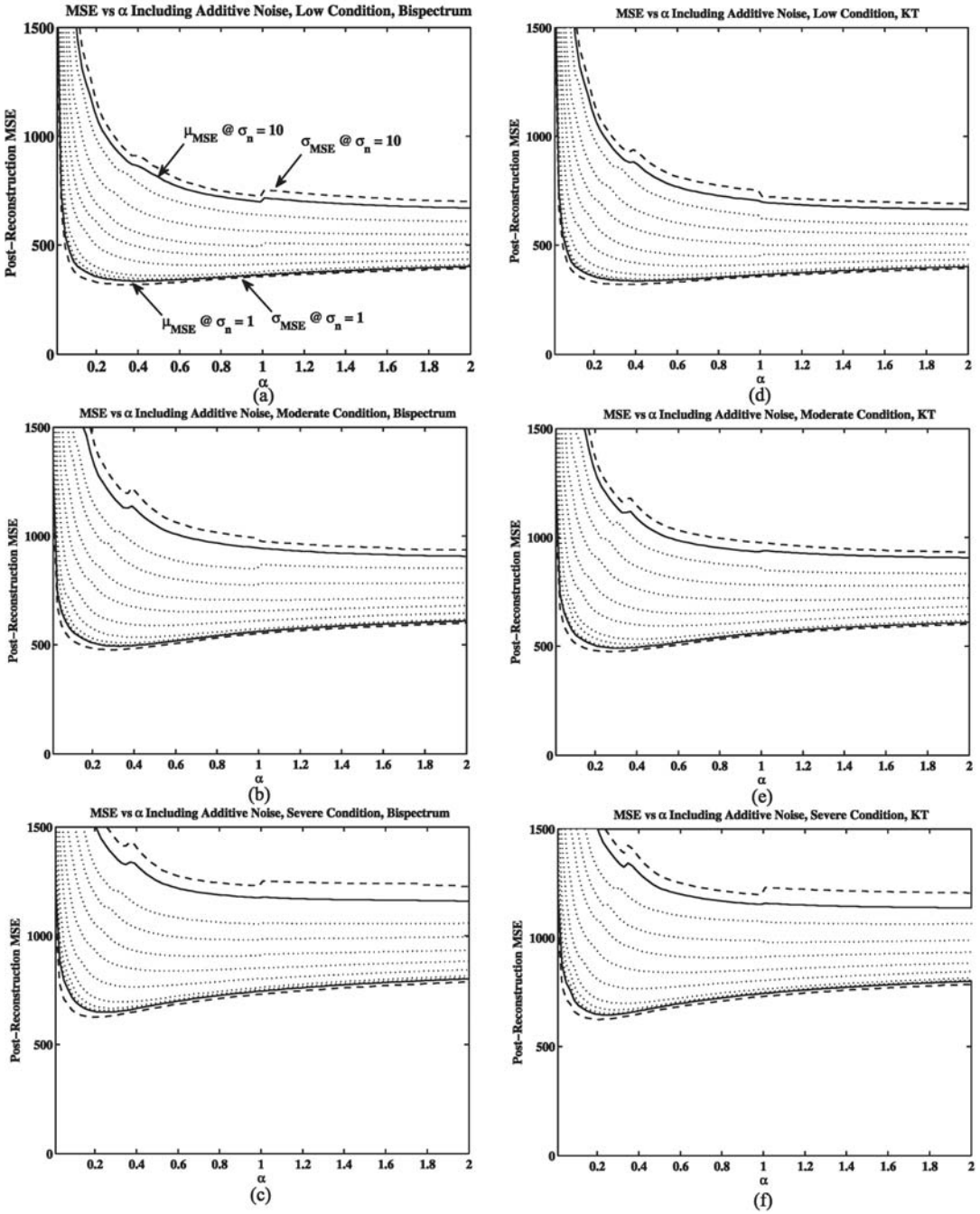

Figure 3.3: Evaluation of the effect on the post-reconstruction residual MSE observed by varying α for the bispectrum (a) "Low", (b) "Moderate", and (c) "Severe" turbulence conditions including additive noise, and similarly for the KT in (d), (e), and (f).In each figure, the solid lines represent the mean reconstruction performance for $\sigma_n = 1$ and $\sigma_n = 10$ with the dotted lines indicating the mean performance for $\sigma_n = 2, 3..9$. Dashed lines at the limit of the volume represent the deviation for the two extreme cases.

3.5.3 Effect of the estimate of C_n^2 on reconstruction performance

In addition to the noise parameter discussed above, the Weiner filter in Eq. 3.6 also requires an estimate of the blurring function, $\hat{H}_{LE}$. The the long-exposure transfer function in Eq. 3.4 is used here and requires an estimate either of r_0 or C_n^2 and the length of the imaging path. An experienced user would not find it difficult to roughly estimate these parameters by observation of the viewing conditions during acquisition. It may even be possible to accomplish this task automatically. In either case, an exact or optimum estimate is unlikely. Given the data sets represents conditions in the range of $C_n^2 = 10^{-14}$ m$^{-2/3}$, it is reasonable to assume that the user can estimate turbulence strength within plus or minus an order of magnitude and vary the estimate over this range to determine an optimum value. In this case, C_n^2 is varied over the range of 10^{-15} to 10^{-13} m$^{-2/3}$; values typical of overland conditions during the day near the ground.

In this evaluation, the number of input frames was fixed as $N_f = 50$ allowing for evaluation over $N = 20$ independent reconstructions. The noise parameter was fixed at $\alpha = 0.4$ and $N_p = 5$. Values were recorded in Table 3.2 for the residual MSE at the value of C_n^2 that yielded the minimum residual MSE. The MSE at the theoretical values are recorded in Table 3.3. Note that in each case the minimum value of MSE is available when better seeing conditions are assumed. This discrepancy is most pronounced for the “Low" turbulence condition where the optimum value differs from the theoretical value by 33%. Despite this

Table 3.2
Values of C_n^2 producing the minimum mean MSE in residual reconstruction MSE and the recorded deviation at that value.

Condition	Min. MSE	C_n^2 at Min. MSE 10^{-14} m$^{-2/3}$	Min. σ_{MMSE}
"Low"	318	1.5	11
"Moderate"	483	2.7	12
"Severe"	653	4.5	14

Table 3.3
Value of the mean MSE and deviation in reconstruction performance available when theoretical values are used to estimate the blurring function.

Condition	MSE	σ_{MSE}
"Low"	338	18
"Moderate"	493	17
"Severe"	655	14

sizeable difference, the penalty incurred in MSE is rather small at 6%. At higher turbulence strengths, this effect is less pronounced and examining Fig 3.4 it is evident that there is little if any penalty for over estimating C_n^2 for moderate and severe turbulence conditions. From these results it can be concluded that exact estimates of C_n^2 are only necessary when seeing conditions are favorable and as seeing conditions degrade this parameter has less importance. To reinforce this point, observe that performance is nearly optimum over the range $C_n^2 = 1$ to 3×10^{-14} m$^{-2/3}$ for the "Low" condition, $C_n^2 = 2$ to 5×10^{-14} m$^{-2/3}$ for the "Moderate" condition and for values greater than $C_n^2 = 3 \times 10^{-14}$ m$^{-2/3}$ in the "Severe" case.

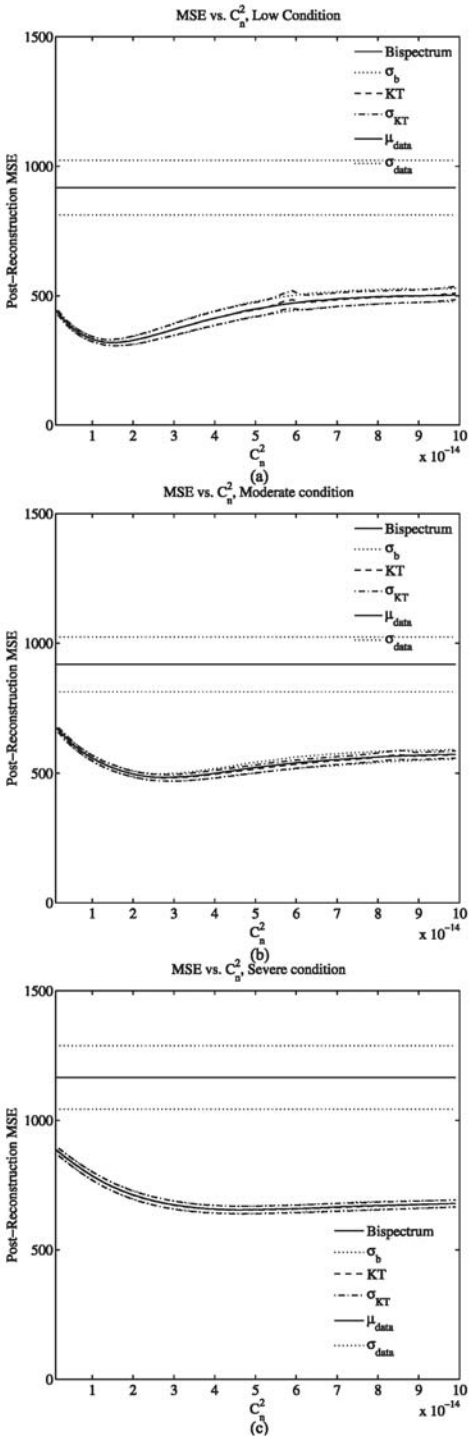

Figure 3.4: Evaluation of the effect on the post-reconstruction residual MSE observed by varying C_n^2 for the (a)"Low", (b)"Moderate", and (c)"Severe" turbulence conditions.

3.5.4 Effect of the estimate of C_n^2 on reconstruction performance including additive noise

Following a procedure identical to that used to evaluate the noise parameter in section 3.5.2 the sensitivity to estimates in C_n^2 was also examined including additive noise. The obvious exceptions being that the best-fit values of α were used in the analysis and the value of C_n^2 was varied to produce the results. These results are presented graphically in Fig. 3.5 separately for the bispectrum and KT phase estimation methods. It is observed that, in general, the presence of noise has the affect of reducing the sensitivity to the value of C_n^2 over the range of values considered.

3.5.5 Effect of the Number of Input Frames on Reconstruction Performance

Input frames used for speckle imaging in astronomical imaging are typically dominated by photon-noise requiring many input frames, between a few hundred to many thousands, to produce an acceptable reconstruction image. It is reasonable to expect that the number of input frames will have a similar importance in horizontal imaging scenarios, though it is likely that far fewer frames will be necessary to achieve an asymptotic level of performance. In thi examination of the importance of this parameter, the residual MSE

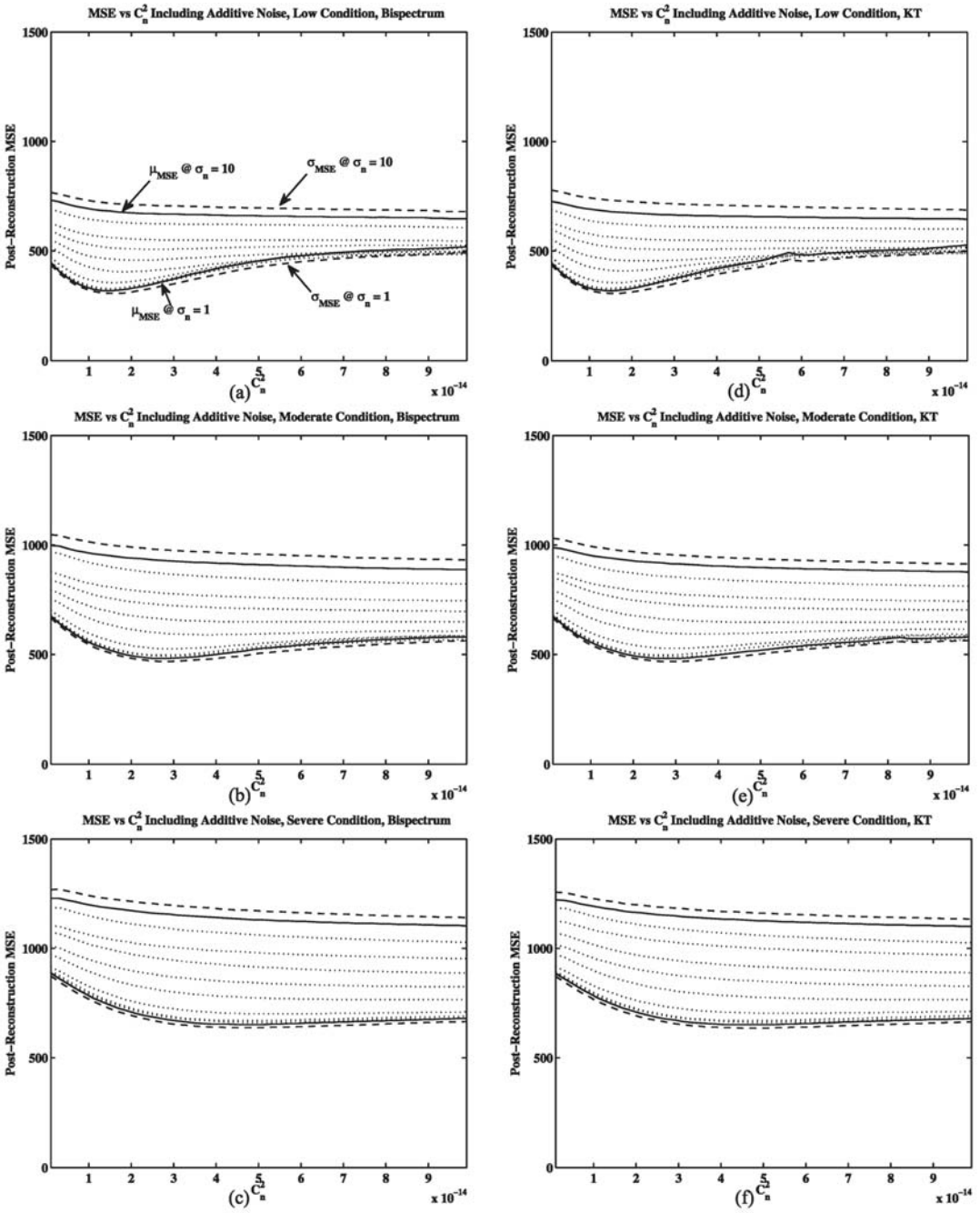

Figure 3.5: Evaluation of the effect on the post-reconstruction residual MSE observed by varying C_n^2 for the (a) "Low", (b) "Moderate", and (c) "Severe" turbulence conditions including additive noise using the bispectrum. The same figures are also included for (d) "Low", (e) "Moderate", and (f) "Severe" conditions using the KT method for phase recovery. In each figure, the solid lines represent the mean reconstruction performance for $\sigma_n = 1$ and $\sigma_n = 10$ with the dotted lines indicating the mean performance for $\sigma_n = 2, 3..9$. Dashed lines at the limit of the volume represent the deviation for the two extreme cases.

for scenarios where between 2 and 25 input frames are supplied to estimator producing $N = 40$ reconstructions. Theoretical values of C_n^2 are used in the Weiner filter and $\alpha = 0.4$. As in previous analysis $N_p = 5$. The result of this evaluation is provided for each turbulence condition in Fig. 3.6

Inspecting Fig. 3.6 it is evident that performance approaches an asymptotic limit near $N_f = 15$ regardless of the turbulence strength. Here the mean residual MSE has been reduced by 43% on average across turbulence conditions and the deviation reduced by 70% compared to the data set mean. Increasing the number of input frames from $N_f = 15$ to $N_f = 25$ provides only an additional 1% improvement in the mean MSE found in reconstructions though the deviation is reduced an additional 7%. The mean and deviation in residual MSE for the three data sets at $N_f = 15$ and $N_f = 25$ are summarized in Table 3.4.

3.5.6 Effect of the Number of Input Frames Containing Additive Noise on Reconstruction Performance

Similar to the treatment of other parameters in this work, when noise, $\sigma_n = \{1, 2, ..10\}$, is added to each input frame performance is maintained relative to the SNR of the input frame. Results of this analysis are presented in Fig. 3.7 for three turbulence cases and separately for the bispectrum and KT methods. The performance is roughly equivalent between estimators with minor differences present at high noise levels. This equivalency

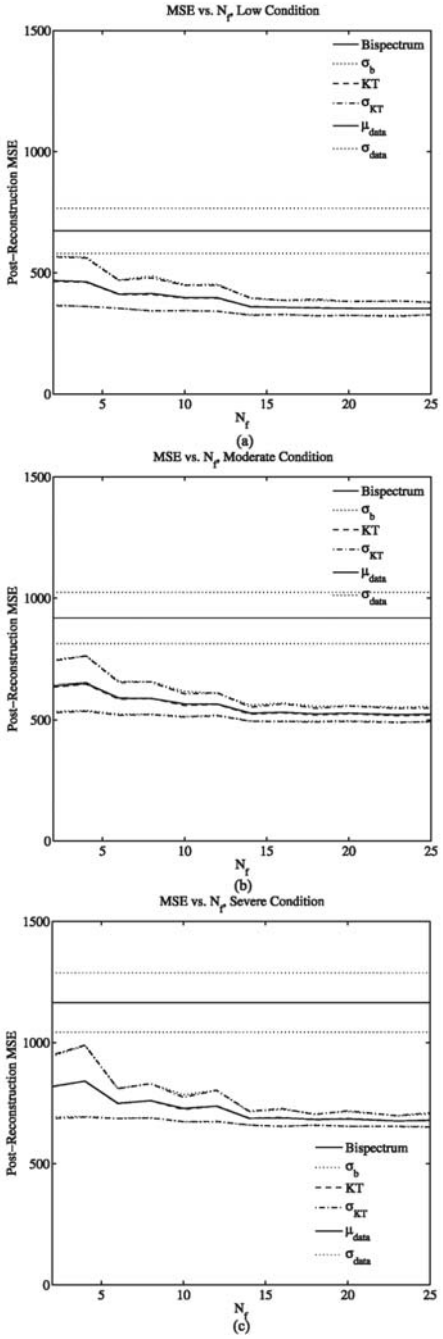

Figure 3.6: Evaluation of the effect on post-reconstruction residual MSE observed by varying the number of input frames for the (a)Low, (b)Moderate, and (c)Severe turbulence conditions.

Table 3.4
A comparison of the available MSE statistics available between $N_f = 15$ and $N_f = 25$.

Condition	μ_{15}	σ_{15}	μ_{25}	σ_{25}
"Low"	357	29	353	26
"Moderate"	531	38	523	31
"Severe"	608	36	678	26

is demonstrated in Fig. 3.8 where the performance of both estimators is examined as a function of additive noise at $N_f = 15$.

3.5.7 Effect of increasing the number of phase estimates on reconstruction performance

From Eq. 3.11 and Eq. 3.12 it is obvious that multiple combinations of $\vec{f}$ and Δf may be used to develop an estimate for the phase at the unknown frequency $\vec{f}'$. Incorporating multiple independent estimates improves the reliability of estimates of the unknown phase. Independent estimates are obtained by making use of additional subplanes in the bispectrum or cross-spectrum by increasing the value of Δf in Eq. 3.7 and Eq. 3.8 for a fixed value of $\vec{f}'$. In this section the effect of increasing the number of independent phase estimates on reconstruction quality is examined. Although more complex phase estimation methods exist [10],[11] a simple averaging of phase quantities is used here. This approach is similar to the standard weighting method [10] with equal weights applied to each estimate.

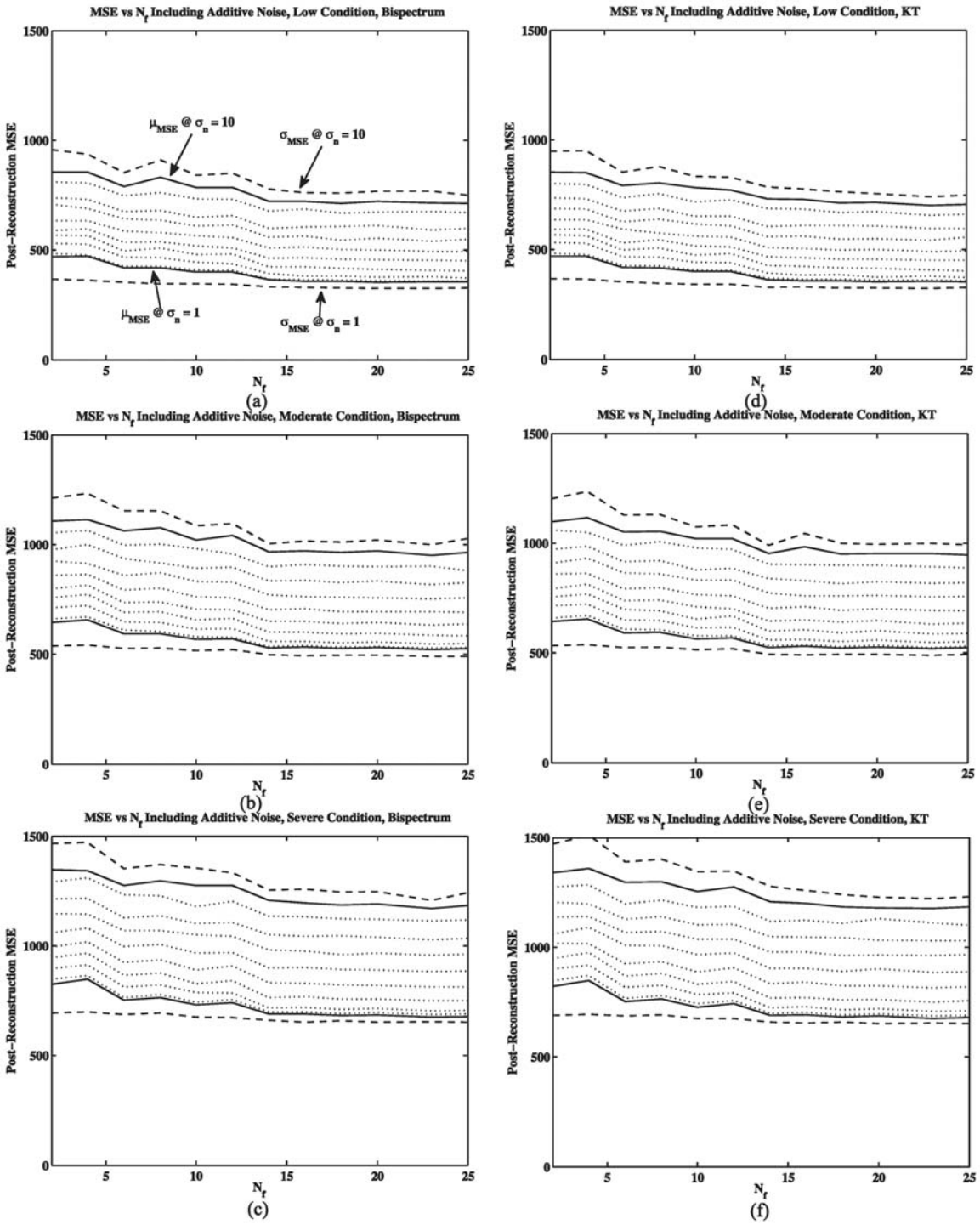

Figure 3.7: Evaluation of the effect on the number of input frames on post-reconstruction residual MSE including noise effects for the bispectrum (a), (b), and (c) and KT (d),(e), and (f) phase estimators. In each figure, the solid lines represent the mean reconstruction performance for $\sigma_n = 1$ and $\sigma_n = 10$ with the dotted lines indicating the mean performance for $\sigma_n = 2, 3..9$. Dashed lines at the limit of the volume represent the deviation for the two extreme cases.

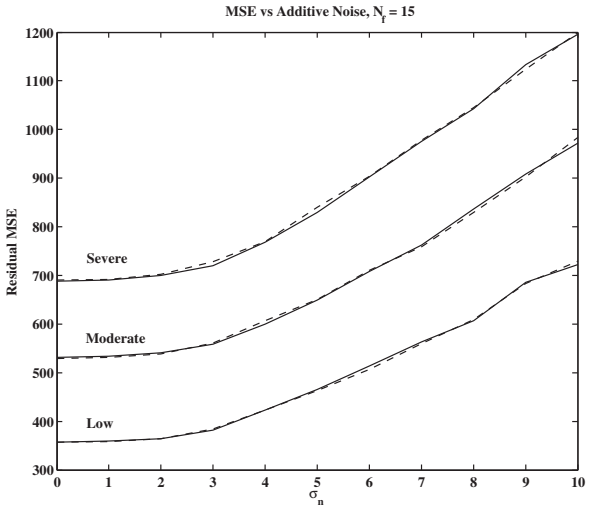

Figure 3.8: Residual MSE as a function of the noise severity for each of the turbulence conditions when $N_f = 15$. Bispectrum - solid lines, KT - dashed.

The results of this analysis are presented in Fig. 3.9. In this figure the number of planes, N_p, in the bispectrum and KT is varied from 1 to 10 with $N_f = 50$, $\alpha = 0.4$ and C_n^2 set to the theory-based simulation values each data set. From Fig. 3.9 it is immediately evident that a majority of the improvement is available when only 2 phase estimates are averaged. This result is not unexpected as the SNR of the bispectrum and cross-spectrum is higher for smaller values of Δf and decreases as the magnitude of Δf increases. For image sets with high SNR the use of additional subplanes reduces the variance in the reconstruction quality but provides little marginal improvement in mean residual MSE. This reduction in variance continues until $N_p = 5$ subplanes.

Including additional phase estimates does not dramatically effect reconstruction quality but it has a significant effect on reconstruction time. Having the option to use fewer

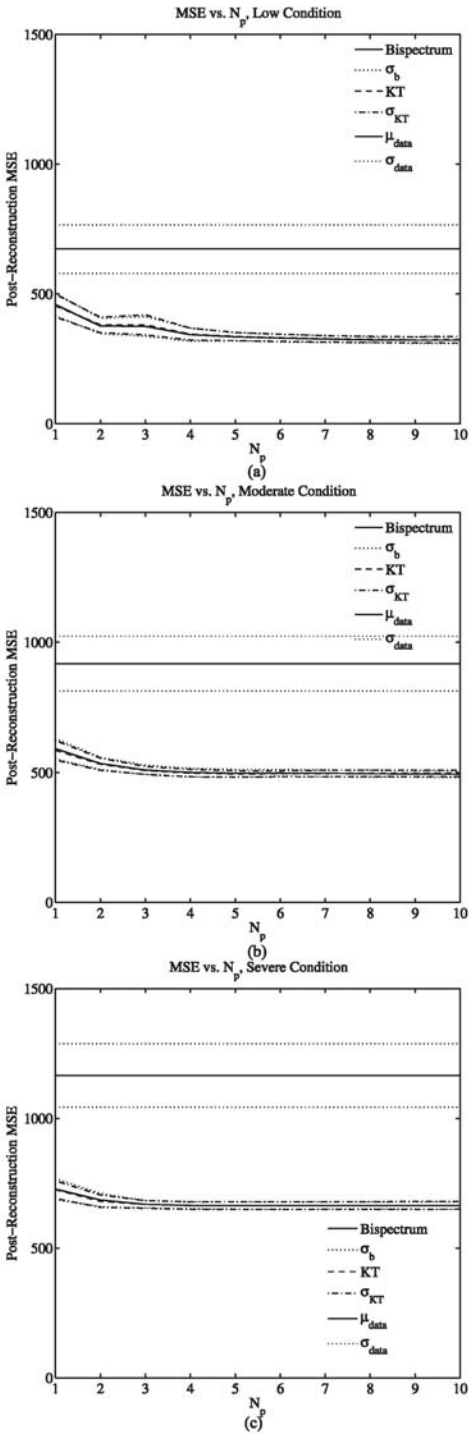

Figure 3.9: Residual MSE as a function of the number of estimates, used to inform the estimated phase at each spatial frequency for the (a) "Low", (b)"Moderate", and (c) "Severe" turbulence cases. Results are presented for the bispectrum (solid) and KT (dashed) in each figure.

phase estimates allows the effective available frame rate to be increased by decreasing the reconstruction time. In Fig. 3.10 this dependence is characterized for both phase recovery methods. Two conclusions result from this analysis. First, for both methods reconstruction time increases as the square in the number of phase estimates considered. Second, the time required by the bispectrum to produce a reconstruction is roughly double that of the KT method. From the first observation it is possible conclude that using more than 5 phase estimates in speckle-imaging systems makes little sense. The second finding is more interesting as the bispectrum is traditionally favored in the speckle imaging of space objects. However, the analysis presented in this chapter indicates that reconstructions produced by each method are equivalent under daylight horizontal imaging conditions. The other chief advantage of the bispectrum, namely the shift-invariance, is negated by the nature of the extended scenes being reconstructed. For any extended scene registration is required regardless of the estimator used in order to provide a consistent version of the scene. Considering the increase in reconstruction time associated with the bispectrum, and in this absence of any other benefit, the Knox-Thompson method should be considered for use in speckle-imagers assigned to horizontal imaging applications.

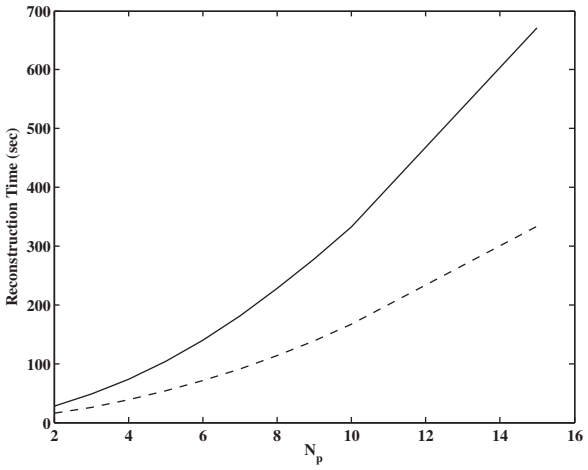

Figure 3.10: Phase reconstruction time as a function of the number of independent phase paths used to object spatial frequency for the bispectrum (solid) and KT methods (dashed).

3.5.8 Effect of increasing the number of phase estimates on reconstruction performance including additive noise

The examination of the number of phase estimates as a design parameter is completed by analyzing the variation in performance in the presence of additive noise. After all the, purpose of using of additional phase estimates is to improves reconstruction performance when using low SNR input frames. Similar to the analyses of the other free-parameters, additive noise with $\sigma_n = \{1, 2, ..10\}$ was added to the image frames and the reconstruction performance evaluated as the number of phase estimates varied. The result of this analysis is best interpreted graphically. Referring to Fig. 3.11, there is little improvement available by incorporating more than $N_p = 5$ phase estimates. In contrast to the noise-free case, it is

necessary to include at least 4 estimates to ensure reconstruction performance at moderate to high noise levels ($\sigma_n > 5$).

3.6 Conclusion

To be of practical use, image reconstruction methods used in automated of man-portable horizontal imagers must maintain their performance over a range of input conditions. In addition to the severe anisoplanatic distortions experienced in these scenarios, imaging methods must be robust to uncertainty and variation in a number parameters controlled by the designer or user. Based on the analysis in this chapter, it can be concluded that speckle imaging techniques satisfies the stated definition for robustness over the conditions evaluated. The analysis presented here also results in a number of recommendations regarding the design of practical speckle imaging systems. Of the parameters considered, estimates for turbulence strength, in terms of C_n^2 or some other measure, are likely to have the largest associated uncertainty. However, even a rough estimate of turbulence strength allows for nearly optimum reconstruction quality. In fact, there may be at most a weak relationship between the turbulence conditions and the estimate for C_n^2 that produces the best reconstruction quality. The results presented here also suggest that the number of input frames be limited to $N_f = 15$ if operation requirements require a high frame-rate. Similarly, under high SNR conditions the number of phase estimates may be limited to $N_p = 2$, though $N_p = 4$ is recommended to preserve a certain level of noise immunity. Finally, most values

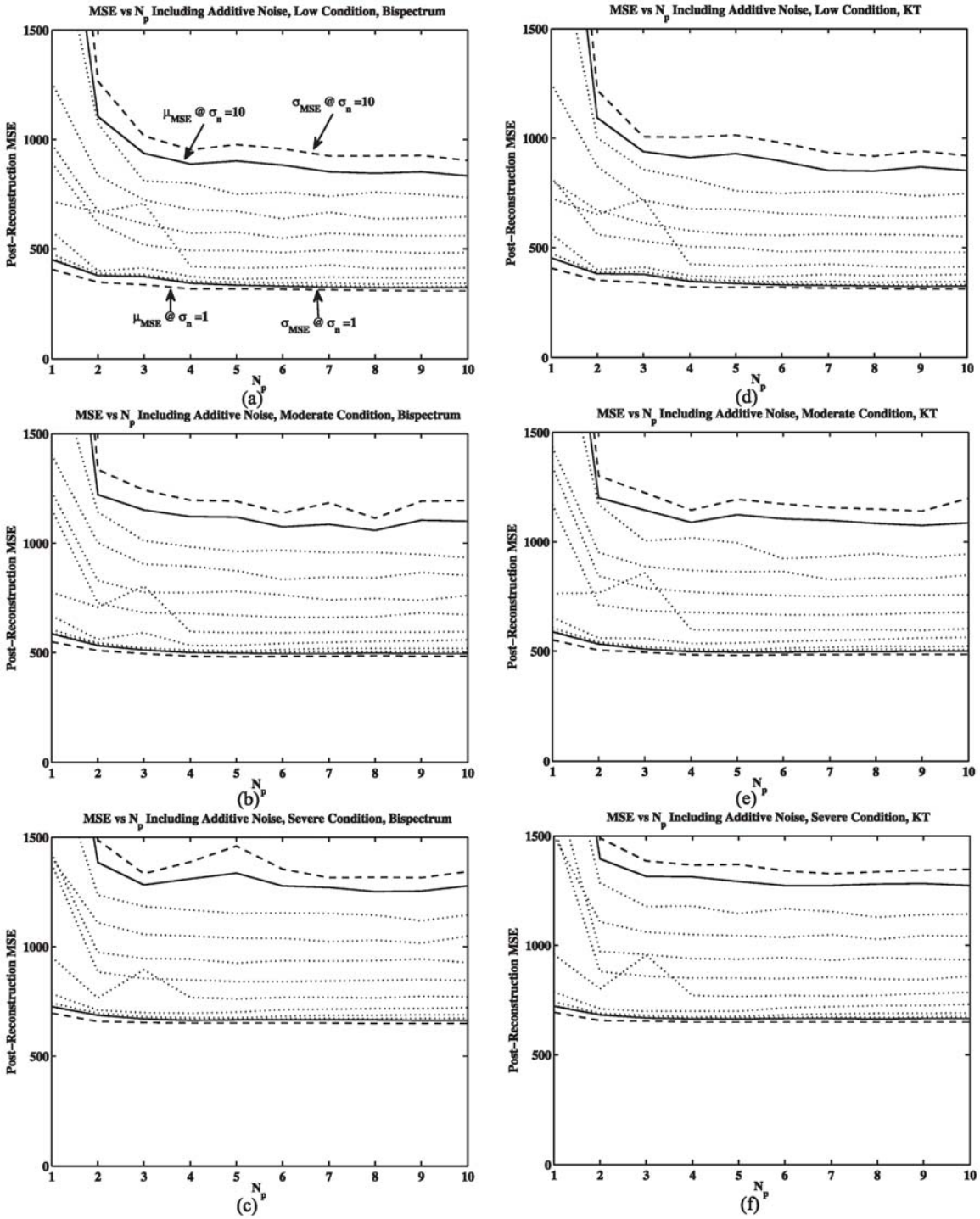

Figure 3.11: Residual reconstruction MSE as the number of phase estimates is increased in the presence of additive noise. In each figure, the solid lines represent the mean reconstruction performance for $\sigma_n = 1$ and $\sigma_n = 10$ with the dotted lines indicating the mean performance for $\sigma_n = 2, 3..9$. Dashed lines at the limit of the volume represent the deviation for the two extreme cases.

of the Weiner filter noise parameter, α, provide near optimum reconstruction performance. This allows the value to be tuned over a broad range according to user preference. Though it may be desirable to calibrate an optimal value for α specific to an imaging system.

Perhaps the most interesting result of this work is the recommendation that the KT method be used in place of the bispectrum for horizontal imaging applications. The KT method provides performance equivalent to bipectrum but requires half the time to produce an image. Bearing in mind that weight, power-consumption, and cost are important factors in the design of horizontal imagers the KT should receive serious consideration for use in these systems. As a final qualitative argument to this point, reconstructions based on the design suggestion listed above are provided in Fig. 3.12. In this figure example input frames are provided in the left column, reconstruction using the bispectrum method are presented in the center column, reconstructions using the KT method are provided in the right column. Images in the top row of the figure are for the "Low" turbulence condition, with the "Moderate" and "Severe" conditions represented in the middle and bottom rows respectively.

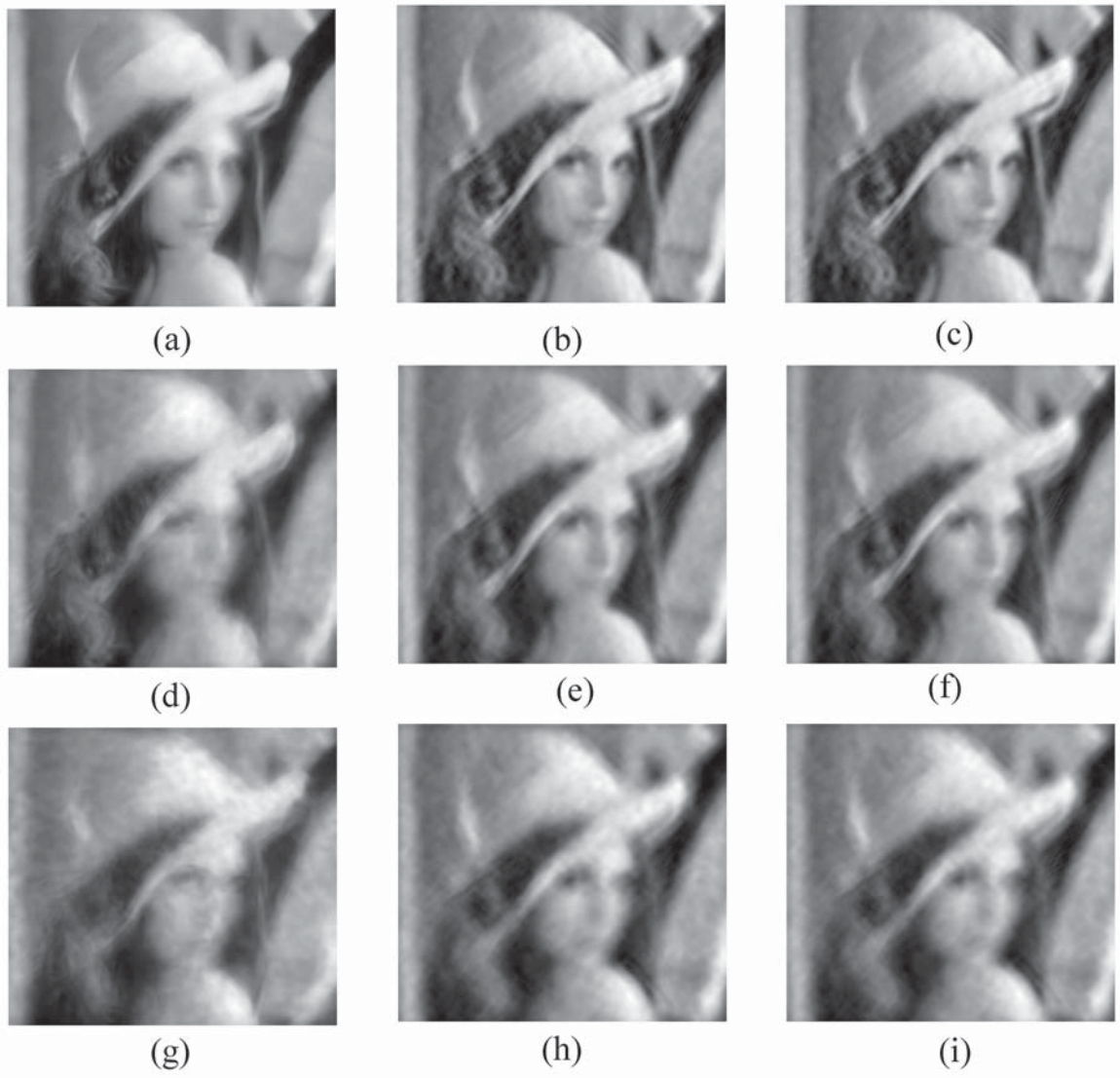

Figure 3.12: Example input frames for the (a)"Low", (d)"Moderate", and (g)"Severe" turbulence cases. Reconstructions using $N_f = 15$,$N_p = 4$,$\alpha = 0.4$, and the optimum values of C_n^2 listed in Table3.2 are presented for the bispectrum (b),(e),(h) and KT (c),(f),(i).

Chapter 4

Blind Image Quality Metrics for Optimal Speckle Image Reconstruction in Horizontal Imaging Scenarios

[1]

[1]The material contained in this chapter has been submitted for publication in the journal Optical Engineering. See Appendix C for documentation of permission to republish this material.

4.1 Introduction

Using man-portable imaging systems, it is possible to monitor sizable areas from remote vantage points over long horizontal or slant paths. Atmospheric turbulence along these paths introduces anisoplanatic distortions which corrupt acquired images, severely limiting their ability to gather useful information. Image processing methods are currently being developed which can counteract these effects. To be considered capable, horizontally-tasked imaging systems must provide distortion-free imagery of remote scenes to operators who are unlikely to be familiar with the underlying image processing algorithm. Horizontal imagers used in portable systems must also be able to meet challenging Size, Weight, and Power (SWaP) requirements. Implicitly, these requirements limit the algorithms to those that are both computationally efficient and able to provide real-time, or near real-time, imagery to the end user.

Of the many methods proposed to tackle this problem [28],[29],[20], techniques based on speckle imaging have shown considerable promise in that they operate capably over a range of imaging conditions when operated by novice users [30],[27]. In addition, real-time embedded image processing systems based on speckle imaging methods are available commercially [31]. An open problem specific to the application of speckle imagers to horizontal imaging scenarios is the need to estimate of the atmospheric blurring function in the absence of natural or man-made point sources. Accurate estimation of this quantity

is necessary to provide an optimum reconstruction of the scene. If too much blurring is assumed, processing artifacts and noise will dominate the reconstructed images. On the other hand, if the too little blurring is assumed recovered images will lack sharpness. In a Chapter 3, the impact of estimating turbulence strength in terms of C_n^2 was evaluated assuming a blurring function based on the theoretical long exposure atmospheric Optical Transfer Function (OTF) and assuming the imaging path length was known. As an outcome of this work, it is known that estimates of C_n^2 within an order of magnitude of the true value result in reconstructions which were similar to the best reconstructions available from the estimator both in visual quality and in terms of Mean Squared Error (MSE). Unfortunately, estimating C_n^2, even to an order of magnitude is likely beyond the ability of novice operators.

Considering the wide range of C_n^2 values which result in optimum, or nearly optimum reconstructions, it is reasonable to wonder if other quality metrics may be used to autonomously tune the value C_n^2 used to atmospheric OTF model. One possibility would be to use image sharpness metrics similar to those proposed for the imaging of space objects in adaptive optics systems [34]. Image sharpness is certainly appropriate when imaging objects comprised of many edges. However, natural scenes are comprised of objects made up of edges and complex textures. Relative to speckle imaging, metrics based on image sharpness may prefer OTF estimates associated with turbulence strength resulting in over-expression of reconstruction artifacts and noise.

Recent works in the area of Blind Image Quality (BIQ) assessment [35], [36], [37] provide a promising alternative to metrics based purely on image sharpness. Most of these methods rely upon models of the Human Visual System (HVS) or Natural Scene Statistics (NSS) [37] to judge relative image quality. In each case, the aim is typically to provide an alternative to the the MSE, which often fails to correlate with Mean Opinion Scores (MOS) indicated by human evaluators [38]. This failure is particularly of common when image defects are due to lossy compression schemes. Consequently, the majority of these methods are based on the assumption that defects in the image are due to image compression. As one might expect, these metrics excel at detecting compression specific artifacts like blocking, but are less sensitive to the residual blur from poor estimates of atmospheric blurring. A related novel BIQ technique relies on the concept of anisotropy [39] in image entropy in order to assess quality. For brevity this metric is referred to as the ABIQ metric for Anisotropic BIQ. This method benefits from being agnostic to imaging artifacts while emphasizing edge sharpness without penalizing textures which may be evaluated as blurry.

In this work, the use of BIQ metrics based on edge detection [34] and anisotropy in image entropy [39] are evaluated for the purpose of providing reconstruction that is equivalent to the Minimum Mean Squared Error (MMSE) reconstruction of the scene available using speckle imagers. Both the image sharpness metric and the ABIQ metrics are found able to provide near optimal reconstruction using previously obtained simulated imagery and imagery collected in the field. In particular, optimizing image quality via the image sharpness method resulted in reconstructions that varied from the MMSE by less than 1%

in most of the cases evaluated.

The remainder of this paper is organized as follows, in section 4.2 a brief summary of speckle imaging techniques is provided as well as a description of the BIQ metrics utilized in this paper. In section 4.3 the methods used to assess the suitability of these blind measure in determining image quality are discussed with respect to the MMSE using both a simulated data set [40] and field data [19]. Results are discussed in Section 4.4 with conclusions and suggestions for future work are provided in Section 4.5.

4.2 Background

4.2.1 Speckle Imaging

Speckle imaging methods attempt to reconstruct a representation of a static scene from multiple turbulence corrupted images of that scene. Recovery is achieved via estimation of the object Fourier amplitude and phase from the statistics of the Fourier transform of the image ensemble. Estimation of these quantities occurs in separate steps beginning with the 2-D Fourier transform of each image frame. The image spectrum for a frame $n = 1,2..N$ in the ensemble $I_n(\vec{f})$, can be considered the product of a deterministic object spectrum, $O(\vec{f})$, OTF, $H_{atm,n}(\vec{f})$, which accounts for both the diffraction-limiting effects of

the imaging system and the random distortion caused by the atmosphere, or

$$I_n(\vec{f}) = H_{atm,n}(\vec{f})O(\vec{f}) \tag{4.1}$$

The object amplitude, $O(\vec{f})$, is recovered from the expected value of the Power Spectral Density (PSD) of the ensemble

$$\langle |I_n(\vec{f})|^2 \rangle = \langle |H_{atm,n}(\vec{f})|^2 \rangle |O(\vec{f})|^2. \tag{4.2}$$

using a pseudo-Weiner inverse filter

$$|\hat{O}(\vec{f})|^2 = \frac{\langle |I(\vec{f})|^2 \rangle_n}{\langle |H_{atm,n}(\vec{f})|^2 \rangle_n + \alpha} \tag{4.3}$$

In Eq. 4.3, α is a noise regularization parameter and $\langle |H_{atm,n}(\vec{f})| \rangle$ is the ensemble average atmospheric OTF, including diffraction effects of the imaging system, over n image frames. The ensemble average, or Long Exposure, atmospheric OTF is often obtained by observing a point-source, such as a star in the case of astronomical imaging over many multiples of the characteristics time scale of the turbulence; theoretical models are also used. After filtering in Eq. 4.3 the object amplitude is recovered from the PSD by taking the root of $|\hat{O}(\vec{f})|^2$.

Phase recovery in speckle imaging systems is accomplished using either the cross-spectrum or the bispectrum of the ensemble image spectrum to estimate the object phase. The

bispectrum, being the more commonly used, is utilized for phase recovery in this work. The image bispectrum is a complex, four dimensional data object defined as $B(\vec{f},\Delta\vec{f}) = I(\vec{f})I(\Delta\vec{f})I^*(\vec{f}+\Delta\vec{f})$ where Δf indicates the offset or plane of the bispectrum. The object phase may be recovered from the bispectrum by first considering that the ensemble average atmospheric bispectrum transfer function is real valued [18, p.153]. Accordingly, the expected value of the bispectrum phase is identical to the object bispectrum. The object phase is then recovered from the ensemble average bispectrum phase of the input image frames by recursion. Considering only the complex object phase, the phase at an unknown frequency, $\phi_o(\vec{f}')$ is recovered using previously recovered phase information at $\phi_o(\vec{f})$ and $\phi_o(\Delta f)$ and the average bispectrum phase,

$$\phi_o(\vec{f}') = \phi_o(\vec{f}) + \phi_o(\Delta f) - \langle \phi_B(\vec{f},\Delta f)\rangle_n \tag{4.4}$$

Recursion begins at the origin, $\vec{f} = 0$, where owing to the real nature of each image as a signal, the phase must be zero. Another phase value is necessary to begin the recursion. Therefore, it is also necessary to set the values of the object phase adjacent to the origin to zero. Due to this last constraint, the reconstructed object image is centered about the centroid of the intensity distribution in the image and may be improperly registered within the image frame. Fortunately, this defect is easily dealt with as a post-processing step. Further, as the recursion moves out from the origin, multiple combinations of $\vec{f}$ and Δf satisfy the relation in Eq. 4.4, $\vec{f}' = \vec{f} + \Delta f$. It is common here to use multiple recursion paths in order to improve the estimate of the object phase. In this work, up to 5 recursion

paths are averaged to estimate the object phase at each spatial frequency. Other, more optimal methods of phase recovery [10], [11] are available but their examination is not pertinent to the work presented here. Once the object amplitude and phase have been estimated the combination of the two quantities is combined. The inverse Fourier transform of the combination

$$\hat{i}(x,y) = \mathscr{F}^{-1}\{|O(\vec{f}|\exp\{j\phi_o(\vec{f})\}\} \tag{4.5}$$

provides and estimate of the object image.

While phase recovery using speckle imaging requires no knowledge of the turbulence conditions, recovery of amplitude information in Eq. 4.3, requires an estimate of the atmospheric OTF. In most cases relevant to horizontal imaging, exact knowledge of the atmospheric OTF is unlikely unless a natural or artificial point source is present in the image frame. Instead, it is common to use an estimate of the atmospheric OTF based on theoretical models. Assuming the uniform turbulence strength along the imaging path, the ensemble average atmospheric OTF $\langle|\hat{H}_n(\vec{f})|^2\rangle_n$, in Eq. 4.3 may be replaced with the theoretical long exposure atmospheric OTF [18, pg.87]

$$H_{LE}(\vec{f}) = \exp\left\{-\frac{1}{2}6.88\left(\frac{\lambda D|\vec{f}|}{r_0}\right)^{\frac{5}{3}}\right\} \tag{4.6}$$

in terms of the imaging system aperture size, D, wave number, k. In Eq. 4.6, $r_0 =$

$(0.16C_n^2k^2L)^{-\frac{3}{5}}$ is the atmospheric spatial coherence radius, or Fried parameter with imaging path length L and wavenumber k. The theoretical model in Eq. 4.6 provides an excellent match to experimental data [33], and assuming C_n^2 and L are known the object amplitude may be recovered via Eq. 4.3. In practice, while the path length, L, may be known, the same is not true for C_n^2. One way of dealing with this dilema is to vary C_n^2 parametrically in Eq. 4.6 about an esitmate and use a quality metric, such as the MSE to choose the highest quality image. Unfortunately, the MSE and most other proven image quality metrics require prior knowledge of the uncorrupted scene. An alternative is the use of certain blind or no-reference image quality metrics to perform the same tasks. A summary of the measures considered in this work is provided in the next section.

4.2.2 Measures of Image Quality

The quality of speckle image reconstructions in this work is assessed using three image quality metrics. One of these metrics, the MSE, is non-blind or full reference and is used as a reference to compare the performance of the other metric. Here, the MSE is defined in terms of the normalized intensity value per pixel relative to a diffraction limited reference image, $o(x,y)$. For a reconstruction $\hat{i}(x,y)$ of size $x = \{1,2,..M\}$ by $y = \{1,2,..N\}$ pixels

$$MSE = \frac{1}{MN}\sum_{m=1}^{M}\sum_{n=1}^{N}|\hat{i}(x,y) - o(x,y)|^2 \tag{4.7}$$

For the purposes of this paper the optimal reconstruction is defined, somewhat arbitrarily, as the image among a set of candidates with the MMSE. The goal then, in using blind measures of image quality, is to identify the MMSE image among a set without the need for a reference. These other metrics, based on image sharpness and image anisotropy are blind, or no reference, measures.

In other areas involving the image recovery in the presence of atmospheric turbulence image sharpness is used as a metric to determine reconstruction quality. In adaptive optics applications, for example, image sharpness metrics may be used to optimize the commands sent to a deformable mirror in order to compensate for turbulence effects. In a survey of the metrics, Muller [34], identified a number of metrics suitable for this purpose. One such image sharpness metric is defined as

$$S_4 = \int \left| \frac{\partial^{(a+b)} i(x,y)}{\partial x^a \partial y^b} \right|^2 \tag{4.8}$$

where a, b are the order of the partial derivatives in spatial coordinates x, y of object intensity distribution i. In this same work, Muller and Buffington also show that this metric is maximized when atmospheric effects have been counteracted, though noise effects are not considered in their analysis. Also, when $a, b = 1$, Eq. 4.8 is equivalent to the integral over the Laplacian operator commonly used for edge detection in image processing applications. Using familiar notation, this metric may be expressed discretely for an image

of dimensions M,N, as

$$\sum_{M}\sum_{N}\left|\nabla^2 i(x,y)\right|^2 \tag{4.9}$$

To avoid the noise sensitivity resulting from the derivative in Eq. 4.9 it is common convolve the image with a Gaussian filter

$$h_g(x,y) = \exp\left\{\frac{-(x^2+y^2)}{2\sigma^2}\right\} \tag{4.10}$$

prior to computing the Laplacian. This combination of Gaussian filter and edge detection using the Laplacian is commonly referred to as the Laplacian of Gausssian (LoG) filter. In this work, the summation over a LoG spatial filter of size 10 and $\sigma = 0.5$ applied to a candidate image is used as a method to determine image quality. Due to its similarity to various edge-detection methods, this metric is referred to simply as the "Edge" BIQ metric.

A recognized shortcoming of the MSE as an image quality metric is that it consistently fails to correlate with the MOS [38] indicated by human test subjects. This deficiency has motivated in research into quality metrics which are modeled on the response of the HVS[37]. As mentioned in Section 4.1, a good number of these metrics are focused on evaluating the quality compressed images. The anisotropic blind image quality measure (referred to in this work as ABIQ) proposed by Gabarda and Cristobol [39] is also inspired by the HVS response and is based on the assumption that framed, natural scenes are

composed of regions of texture which are bounded by edges. The non-uniform orientation of these texture region leads to an anisotropy in the directional entropy in a scene. To assess anisotropy in entropy, the pixel-wise local 1-D entropy of an image is first evaluated by finding the normalized Pseudo-Wigner distribution for each pixel $n = 1,2,..NM$ in the image

$$W[n,k] = 2\sum_{t=-T/2}^{T/2-1} z[n+t]z^*[n-t]\exp\{-2j(2\pi t/T)k\} \tag{4.11}$$

along an orientation, θ_s, over a window of size T. The distribution is then normalized to unit energy over spatial frequency variable k,

$$\check{W}[n,k] = \frac{W[n,k]}{\sum_{k=1}^{T} W[n,k]} \tag{4.12}$$

and the Renyi entropy for a pixel, n along a direction θ_S found as

$$R_3[n,\theta_s] = -\frac{1}{2}\log_2\left(\sum_{k=1}^{N}\check{W}[n,k]\right) \tag{4.13}$$

This process is repeated for each pixel and along each desired direction resulting in a map of the distribution of directional entropy in the image.

Image anisotropy is calculated from the average Renyi entropy of the image for each angle,

θ_s

$$\bar{R}[n,\theta_s] = \frac{1}{M}\sum_n R_3[n,\theta_s] \tag{4.14}$$

which is averaged over all angles

$$\mu = \frac{1}{S}\sum_{s=1}^{S} \bar{R}(\theta_s) \tag{4.15}$$

and the image anisotropy found as the standard deviation of the mean direction entropy over each direction S.

$$ABIQ = \left[\frac{1}{S}\sum_{s=1}^{S}(\mu - \bar{R}(\theta_s))\right]^{-1/2} \tag{4.16}$$

In this work, the MATLAB function made available by Gabarda and Cristobol is used to evaluate anisotropy [39]. This function has two input parameters: the window size, T, and the number of directions, S. The default values of $T = 8$ and $S = 6$, or $\theta_s = \{0^\circ, 30^\circ, 60^\circ, 90^\circ, 120^\circ, 150^\circ\}$, were found to provide the best results relevant to this work.

4.3 Methods

In a general sense, the problem outlined in this work is an optimization problem where C_n^2 in Eq. 4.6 is varied while the phase estimate, PSD estimate and other speckle imaging

parameters are held constant. The reconstructed image is then evaluated using one of the quality functions and the best image chosen such that

$$\arg\max_{C_n^2}\{J(I(x,y;C_n^2))\} \tag{4.17}$$

where J is one of the quality metrics described above and $I(x,y;C_n^2)$ is the candidate image. According to the aims of this dissertation, a BIQ metric should reliably provide the same estimate of C_n^2 as the MMSE but without needing a reference image. It is also desirable for the quality functions to have a single, well defined maximum in the neighborhood of the rough estimate, (i.e. near $C_n^2 = 10^{-14}\mathrm{m}^{-2/3}$). Evaluation of the two quality metrics against this criteria is accomplished using two data sets taken from previous works [1], [19]. The first data set is simulated, allowing for comparison of the BIQ metrics to the MSE. The second set is made up of imagery collected as part of field experiments and verifies the performance of the blind metrics, qualitatively, under real world conditions.

The horizontal imaging data set, described in Chapter 2, is composed of 3000 image frames representing 3 turbulence conditions, summarized in Table 4.1 in the range of $C_n^2 = 10^{-14}$ for a 1000 m simulated imaging path. Images are derived from the "LenaŤ" test image which is modeled as a 0.75m object located distant from an imaging system with a 0.1 m aperture. The simulation technique uses a distributed phase screen approach incorporating a simplification of the Fourier split-step propagation model to generate blurring functions which vary as a function of angular separation in the object. The variation in the

Table 4.1
Turbulence parameters for the three simulated data sets. Parameters of $\lambda = 700$ nm $L = 1000$m were used in the simulation and to calculate the value of r_0 in the table under spheric wave propagation conditions.

Label	C_n^2 ($m^{-\frac{2}{3}}$)	r_0 (cm)
Low	2.25×10^{-14}	3.33
Moderate	3.75×10^{-14}	2.45
Severe	5.25×10^{-14}	2.01

atmospheric distortion in the object results in anisoplanatic image distortions and are present in most imagery acquired over long horizontal paths. Example image frames from the simulation model are provided in Fig. 4.1.

The BIQ measures are also evaluated against field data gathered during a recent Laser Communications System (LCS) Experiment [19].The transmitter side of the experiment featured a pinwheel target and a 808 nm laser transmitter. The transmitter station was observed by a 0.3 m aperture telescope over a 3046 m path which extended over both land and water at an elevation of 250 m above mean sea level. A beam-splitter was attached to the back of the receiving telescope which allowed for simultaneous measurement turbulence strength via a Shack-Hartmann Wave Front Sensor (WFS) and imagery via a Point Grey 13S2 CCD camera. Turbulence degraded imagery of the pinwheel target was recorded periodically as part of this experiment during the summer of 2009 under a variety of lighting conditions and turbulence strengths. Unfortunately, the LCS imaging path was oriented approximately along an East-West direction resulting in saturation of the imaging camera during the early morning and late evening when the sun was directly opposed

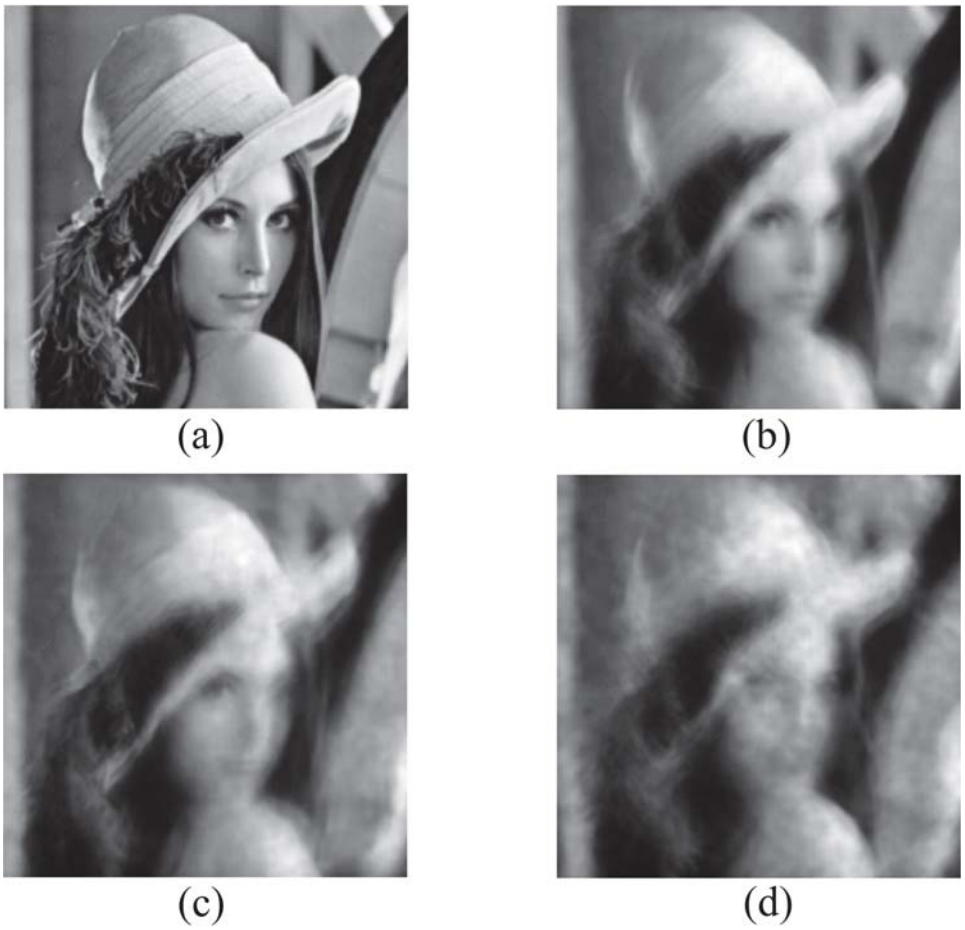

Figure 4.1: Example frames from the simulated data set. Image frames in the panel are for (a) Diffraction-limited, (b) Low, (c) Moderate, and (d) Severe Conditions

to or behind the experiment. Consequently, the only practical imagery acquisition times occurred during the late morning and early afternoon except on cloudy days. During these times the turbulence strength over the imaging path does not vary significantly during with the WFS indicating r_0 values generally between about 2 and 3 cm. In addition, imagery acquired concurrent with WFS measurements could not be used. The presence of the laser transmitter signal in the image frame during these times saturates portions of the

Table 4.2
Date, time and day, and range of WFS measurement near the time of collection for the three data sets considered.

	Date	Time	Range of values in r_0 (cm)
Field 1	2009, July 1	14:00 EDT	4.6 to 5.2
Field 2	2009, July 14	14:00 EDT	2.3 to 2.4
Field 3	2009, July 24	19:00 EDT	1.78 to 2.8

imaging sensor. These saturated areas introduce severe artifacts in the speckle processed images. Background image frames taken immediately before or after WFS measurement are used instead with the understanding that WFS measurements are indicative of the general turbulence conditions and do not represent actual turbulence strength measurements obtained during image acquisition. Three data sets were selected from data collected during the experiment. The date, time and labels applied to the three data sets are provided in Table 4.2 along with the range of average r_0 values over 3, 27 second intervals.

The evaluation of both metrics is carried out using each data set following a common procedure. Amplitude and phase estimates are obtained using speckle imaging techniques as described in Eq. 4.2 and Eq. 4.4. Candidate images are then generated by first inverse filtering the PSD estimate using the pseduo-Weiner filter described by Eq. 4.3 incorporating the estimate of the atmospheric OTF taken as Eq. 4.6 with free parameter C_n^2. The value of C_n^2 in Eq. 4.6 is varied over a range of values and an image generated for each value. Candidate images are then evaluated by the two BIQ metrics. In the case of simulated imagery, the MSE is also evaluated relative to a diffraction-limited reference. The value

indicated by each metric is recorded, normalized and then averaged over each image set. Unconstrained non-linear optimization according to Eq. 4.17 is also performed using the `fminbnd` function in MATLAB [41] to determine an optimum value for each metric. The mean and standard deviation in the predicted optimum value of C_n^2 is recorded and used to evaluate relative performance. In the case of simulated imagery, the difference between the MMSE and the MSE of images indicated to be optimum by the BIQ measures is also recorded.

4.4 Results

The performance of the BIQ measures is first compared to the MMSE using the simulated data set as outlined above. For each turbulence case, $N = 20$ reconstructions were generated from $N_f = 50$ simulation frames. The two blind metrics and the MSE were evaluated as the estimate of C_n^2 used in the inverse filter was varied within an order of magnitude of an estimate, taken to be $C_{n,est}^2 = 10^{-14}$ m$^{-2/3}$. The normalized average of each metric as C_n^2 is varied from 10^{-15} to 10^{-13} m$^{-2/3}$ is shown in Fig. 4.2 for the three simulated data sets. As required, the two blind metrics are continuous and have local maximums near to the MMSE.

The true local optimums indicated by each metric were found using unconstrained nonlinear optimization in MATLAB [41] and are summarized in Table 4.3. Values of C_n^2

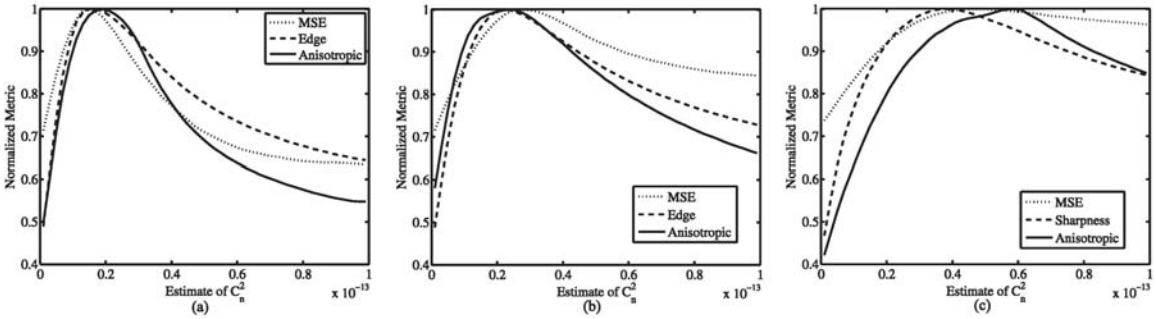

Figure 4.2: Normalized image quality as evaluated by the MSE, Edge, and ABIQ metrics as the estimate of C_n^2 is varied from $10^{-15}\text{m}^{-2/3}$ to $10^{-13}\text{m}^{-2/3}$. The values indicated by each metric are normalized and then averaged over $N = 20$ evaluations derived from reconstructions based on simulated turbulence degraded imagery in (a) "Low", (b) "Moderate", and (c) "Severe" turbulence conditions in the region of $C_n^2 = 10^{-14}$ m$^{-2/3}$ for a path length of $L = 1000$ m

as predicted by the Edge metric differed by 0.13, 0.60, and 1.03×10^{-14} m$^{-2/3}$ for the "Low", "Moderate" and "Severe" turbulence cases relative to the MMSE value. Optimum values for the ABIQ metric differed from the MMSE by 0.45, 0.47, and 0.29^{-14} m$^{-2/3}$ over the same data sets. Over the data sets evaluated, the accuracy of the Edge metric relative to the MMSE decreased as turbulence strength increased while the ABIQ metric proved more accurate for the same images. Across all turbulence strengths, estimates provided by the Edge metric were more precise with deviations about the mean value of $\frac{\sigma}{\mu} = 0.06, 0.12, 0.15$ for the "Low", "Moderate" and "Severe" simulation cases. Though this deviation also increases with turbulence strength, variability in the estimates provided by the ABIQ metric did not show a dependence varying by $\frac{\sigma}{\mu} = 0.16, 0.28, 0.29$ over the same inputs.

Of course, the optimum value of C_n^2 is secondary to the quality of the image reconstructions

Table 4.3
Mean estimates of C_n^2, for $N = 20$ optimizations, which provide the optimum quality image reconstruction as measured using the MSE, Edge, and ABIQ metrics.

	MMSE 10^{-14} m$^{-2/3}$	Edge 10^{-14} m$^{-2/3}$	ABIQ 10^{-14} m$^{-2/3}$
Low	1.490	1.618	1.941
Moderate	2.813	2.215	2.342
Severe	4.913	3.881	4.624

relative to the MMSE. In Table 4.4 the mean and standard deviation in the MSE of the optimum reconstruction indicated by the two blind metrics are compared to the MMSE value. Mean values vary by about 1.1% for optimum reconstruction as indicated by the Edge metric and 2.5% for the ABIQ metric. Similar to estimates of C_n^2, the deviation from the MMSE decreases using the ABIQ metric as relative turbulence strength increases. Though, in all cases, the Edge metric provided estimates closer to the MMSE with less variability. Examples of the optimum image reconstruction as predicted by each metric are shown in Fig. 4.3. While only minor differences exist between the images in each group, reconstruction artifacts, manifested as ringing around sharp edges, are observed to be more pronounced in the optimum reconstructions chosen by the Edge metric relative to the MMSE.

Table 4.4
Mean and standard deviation in the MSE of the optimum reconstruction predicted using the Edge and ABIQ metrics compared the MMSE

	MSE		Edge		ABIQ	
	μ	σ	μ	σ	μ	σ
Low	317.49	10.45	319.61	12.07	327.75	17.52
Moderate	482.45	13.46	490.77	11.91	496.25	17.25
Severe	653.39	14.33	659.28	13.94	662.61	14.34

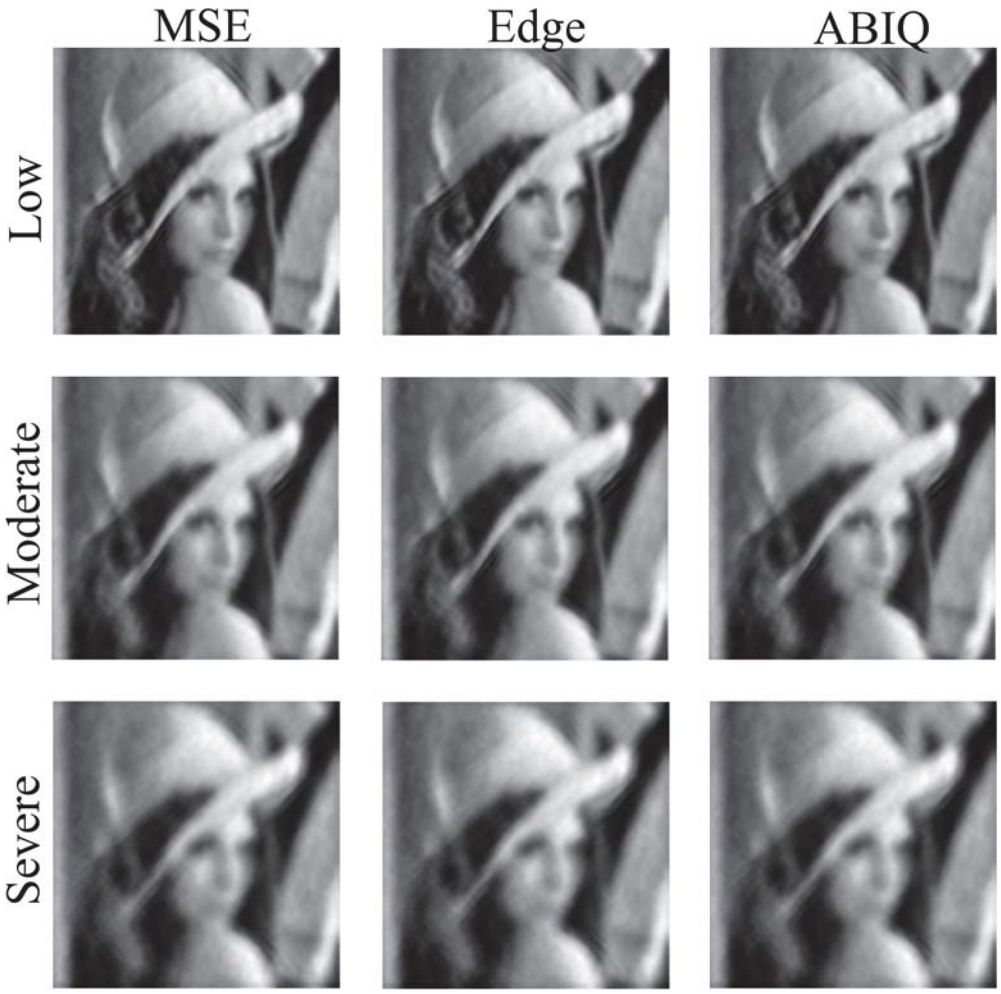

Figure 4.3: Example images frames and reconstructions indicated to be the optimum by each metric for Low, Moderate, and Severe turbulence cases

4.4.1 Field Data

Empirically, the proposed blind measures are similarly capable to the MSE in evaluating image quality in reconstructions based on simulated turbulence degraded imagery. An exercise, similar to the one described above using simulated imagery, was carried out using the field collected data described in Section 4.3. Each 800 frame data set, representing approximately 27 seconds, was divided into, $N = 16$ image sets containing 50 image frames. As with the simulated data set, C_n^2 was varied as a parameter in the atmospheric OTF to estimate the object amplitude and the resulting image quality evaluated using the two BIQ measures. The value of C_n^2 was varied over a range between 10^{-15} to 10^{-13} $\mathrm{m}^{-2/3}$ with the path length was fixed at $L = 3046$ m. Results are found in Fig. 4.4. As mentioned previously, a small subset of the field data collected during the LCS experiment was suitable for speckle image processing, and turbulence conditions over the remaining sets were all near $r_0 = 2$ cm. These conditions are most similar to those in the "Severe" simulated set. It is also important to point out that the distribution of turbulence along the image path in the experiment is unknown and not likely to be constant. As a result, by varying C_n^2 the total integrated turbulence is estimated and not C_n^2. Still, there are similarities between the simulated and experimental data. In both cases, the performance of the ABIQ improves at higher turbulence strengths. Also, both the "Severe" case in Fig. 4.1(c) and the three field cases in Fig. 4.4 have relatively flat responses compared to the weaker turbulence cases in Fig. 4.1(a),(b).

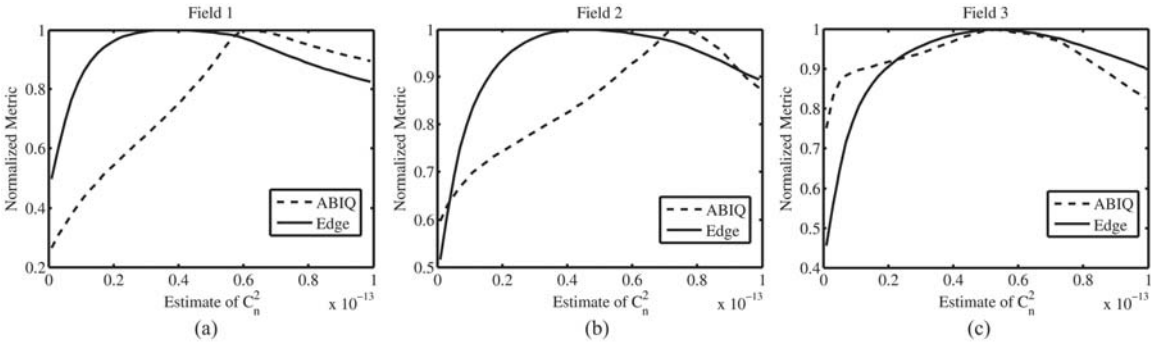

Figure 4.4: Normalized quality metric, averaged over $N = 20$ speckle image reconstructions when the value of C_n^2 in Eq. 4.6 is varied in the range of 10^{-14} m$^{-2/3}$ using LCS field data. Results are for LCS data sets (a) Field 1, (b) Field 2, (c) Field 3

The optimum value of C_n^2 according to the BIQ metric for each data set was also found via the nonlinear optimization procedure described previously. Example optimal reconstructions and corresponding image frames from the source data sets are found in Fig. 4.5. The mean, μ, and standard deviation, σ, in the estimates for each field condition are recorded in Table 4.5. Considering that turbulence condition are not controlled under field conditions, it is reasonable to expect a greater variation in the optimum estimates of C_n^2 compared to those derived from the simulation sets. However, from Table 4.5 the deviation about the mean value for the field data are $\frac{\sigma}{\mu} = 0.07, 0.07$, and 0.15 for the Field 1, 2, and 3 sets respectively using the Edge metric. Values of $\frac{\sigma}{\mu} = 0.09, 0.10$,and 0.02 were recorded using the ABIQ metrics over the same data. By comparison, for the "Severe" simulation data set estimates of C_n^2 varied by 0.15 as a fraction of the mean using the Edge metric and 0.29 using the ABIQ metric. Also consistent with results using simulated imagery, the Edge metric provided estimates with less variability than the ABIQ in most cases, with the exception of the Field 3 data set. In all cases, the values of C_n^2 indicated correspond to values

Table 4.5
Mean and standard deviation in the optimum value of C_n^2 as indicated by the BIQ metrics applied to the three field collected data sets

	Edge (10^{-14} m$^{-2/3}$)		ABIQ (10^{-14} m$^{-2/3}$)	
	μ	σ	μ	σ
Field 1	3.75	0.26	6.06	0.56
Field 2	4.52	0.30	7.74	0.78
Field 3	5.88	0.90	6.89	0.16

of r_0 near 1cm when constant turbulence strength is assumed. Again, this assumption is not likely to apply in this experiment, so values or r_0 are provided only as an indicator of integrated turbulence strength.

4.5 Conclusions

In this chapter, I have shown it is possible to achieve nearly optimal reconstruction quality from speckle imagers applied to horizontal imaging scenarios using blind image quality metrics to assess image quality. Optimal images were chosen by varying turbulence strength in the theoretical model for atmospheric blurring used to recover object amplitude information. When applied to an extensive data set of simulated imagery degraded by the anisoplanatic turbulence, both metrics were able choose images as optimal within 5.5% of the MMSE reconstruction on average. Though both metrics were found to be capable, the Edge-based BIQ metric resulted in images nearer in quality to the MMSE with less variation. The Edge metric also provided more consistent estimates when applied to field

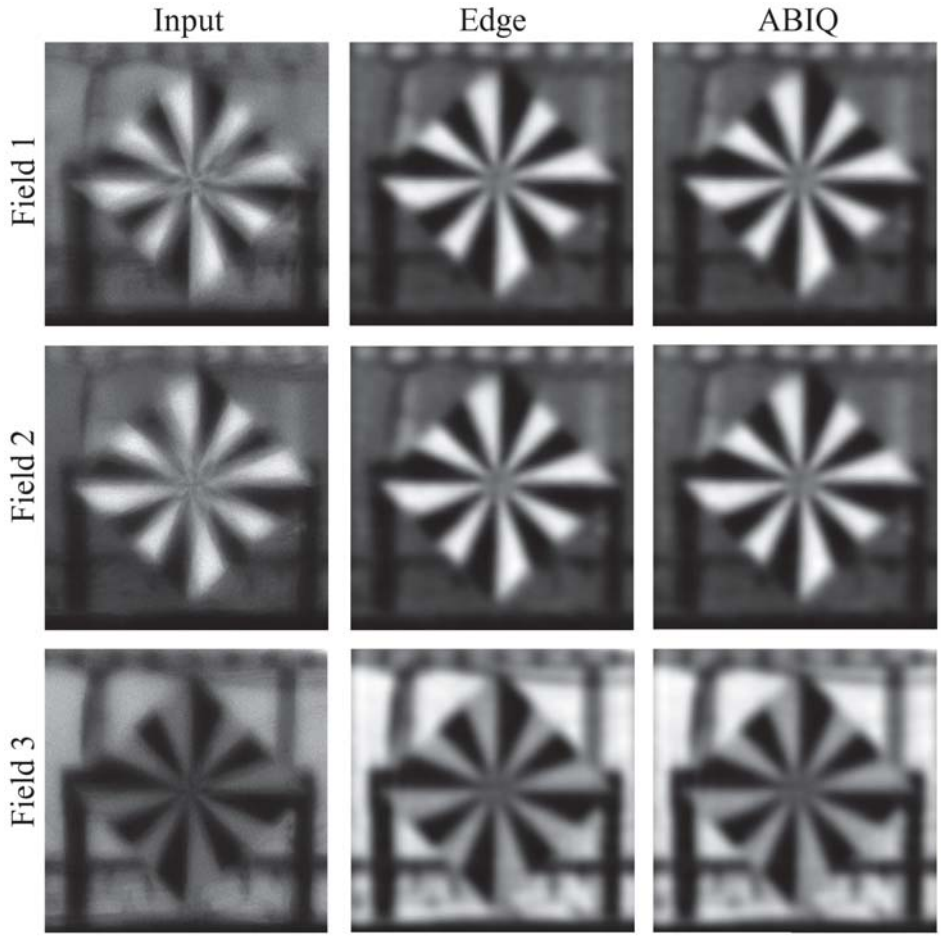

Figure 4.5: Example image frames indicated to be the optimum by each metric for the Field 1, Field 2 and Field 3 data sets

collected data. The Edge metric is also less computationally intensive relative to the ABIQ metric, a significant benefit considering the SWaP restrictions attached to most horizontal imagers.

Although the Edge metric out-performs the ABIQ metric in most measures, Edge metric performance decreased with increasing turbulence strength. Under more severe seeing conditions, not explored here, the ABIQ metric may provide better results. Seeing

conditions present in field-collected data were often severe, but the high contrast, edge-oriented, pinwheel object may have provided an advantage to the Edge metric that would not be present in texture-rich natural scenes. To that point, evaluation of these metrics over a greater variety of target object and seeing conditions, both simulated and experimental would provide additional evidence of their capability. Finally, blind image quality assessment is an area of active research, and while the two metrics evaluated here are representative, many other metrics are available. It is also possible that BIQ measures that are ideally suited for optimal scene reconstruction using speckle imagers over long horizontal paths

Chapter 5

Conclusions

In this dissertation, it was shown that speckle imaging methods are able to reliably provide high-quality reconstructions of images corrupted by turbulence over long horizontal paths. Using a novel simulation model described in chapter 2 a large data set of turbulence corrupted imagery was developed. In chapter 3 this data set was used to select a set of design parameters for speckle imaging systems that provides the highest possible reconstruction quality while minimizing variation in performance and the computation time required to produce recovered imagery. The use of certain BIQ measures was proposed in chapter 4 as a method further reduce design risk and minimize variation in performance due to operator error. Chapter 4 also demonstrated the efficacy of speckle imaging systems applied to field collected data, as opposed to the simulated imagery used in previous chapters. The design recommendations outlined in this dissertation may be

used by engineering teams to develop robust horizontal imagers based on speckle imaging methods.

5.1 Summary of Key Results

The work presented in this dissertation makes a number of important contributions to the field of atmospheric optics. First, a novel method for simulating anisoplanatic image formation over long horizontal paths was developed based on the split-step wave propagation method. Using this simulation model, two extensive data sets of 6000 images were developed based on the "Lena" and "Boats" test images. The distribution of errors, in terms of the MSE in normalized intensity per pixel was shown to follow a log-normal distribution with a mean value that increased linearly with turbulence strength in C_n^2. Using these data sets, it was demonstrated that speckle imaging methods produce images that reduce error, in terms of MSE, by 55% and reduce deviation in image quality by 68% on average across three turbulence conditions. This level of performance is available using only 15 image frames and 4 estimates of the object phase to generate image reconstructions. In addition, it was shown that the bispectrum and KT phase recovery methods produce reconstructions of identical quality in daylight horizontal imaging scenarios and, because it is computationally less expensive, the KT method should be considered for use in embedded implementations. Finally, it was shown that certain BIQ measures may be used in place of the MSE to autonomously optimize the inverse filter used in amplitude recovery.

Specifically, using a simple measure based on image sharpness it was possible to produce imagery within 1% of the MMSE.

5.2 Suggestions for Future Work

As with any good research, there are remain unanswered questions relative to this work that fall outside of the scope of this dissertation but may be of interest to other researchers. Most obviously, it would be worthwhile to compare the performance of speckle imaging systems to other reconstructions methods. Using the simulated image set developed in chapter 2 such a comparison would be both straightforward and informative. To that point, it may be possible to further improve image quality by using the reconstructions from speckle imaging methods as a starting point for iterative multi-frame blind deconvolution methods. These methods are thought to produce higher quality reconstructions, but are also known to have higher computational requirements.

Other ideas for future work in this area involve expansion or improvement of the simulation model. Currently, the image frames generated by the model are independent. Given enough workstation memory, it may be possible to introduce a time correlation between image frames. The correlation time of atmospheric turbulence is on the order of a few millisecond effectively limiting the input frame-rate to less than 100 frames per second under isoplanatic conditions. Creating sets of image frames with time-evolving

turbulence would allow for this limit to be explored under anisoplanatic conditions. Another weakness in the the simulation model is the use of uniformly spaced phase screens. Modifying the model to allow for arbitrary spacings would allow for simulation of differing path-dependent turbulence distributions, including severe slant paths. Other obvious improvements here would involve the creation data sets based on other source images and adapting the simulation code for use on massively parallel systems.

Questions also remain relative to the practical implementation of speckle imaging method in embedded imaging systems. Current embedded systems based on these methods [31] rely on block processing of imagery acquired at high frame rates. My own preliminary work in this area indicates that reconstructions using this method are of lower quality (in terms of MSE) compared to the full-frame methods explored here. The use of block-processing introduces new variables, such as block size and scene recovery, not covered in this work, but are likely to significantly impact image quality. Finally, the additional overhead related using BIQ measures to tune the inverse filter was not explored. As mentioned in section 4.5 there may other BIQ measures which are both more accurate and more efficient that the two measures evaluated.

References

[1] J. P. Bos and M. C. Roggemann, "Technique for simulating anisoplanatic image formation over long horizontal paths," *Optical Engineering*, vol. 51, no. 10, p. 101704, 2012.

[2] J. P. Bos and M. C. Roggemann, "Robustness of speckle-imaging techniques applied to horizontal imaging scenarios," *Optical Engineering*, vol. 51, no. 8, p. 083201, 2012.

[3] G. Taguchi, S. Chowdhury, and S. Taguchi, *Robust Engineering*. McGraw-Hill, 2000.

[4] A. Labeyrie, "Attainment of Diffraction Limited Resolution in Large Telescopes by Fourier Analysing Speckle Patterns in Star Images," *Astronomy and Astrophysics*, vol. 6, p. 85, May 1970.

[5] K. T. Knox and B. J. Thompson, "Recovery of images from atmospherically degraded short-exposure photographs," *The astrophysical journal*, vol. 193, pp. L45–L48, Oct. 1974.

[6] G. Weigelt and B. Wirnitzer, "Image reconstruction by the speckle-masking method," *Optics Letters*, vol. 8, pp. 389–391, Jul 1983.

[7] G. R. Ayers, M. J. Northcott, and J. C. Dainty, "Knox-thompson and triple-correlation imaging through atmospheric turbulence," *Journal of the Optical Society of America A*, vol. 5, pp. 963–985, Jul 1988.

[8] B. M. Welsh and M. C. Roggemann, "Signal-to-noise comparison of deconvolution from wave-front sensing with traditional linear and speckle image reconstruction," *Applied Optics*, vol. 34, pp. 2111–2119, Apr 1995.

[9] M. C. Roggemann, E. L. Caudill, D. W. Tyler, M. J. Fox, M. A. V. Bokern, and C. L. Matson, "Compensated speckle imaging: theory and experimental results," *Applied Optics*, vol. 33, pp. 3099–3110, May 1994.

[10] J. Meng, G. J. M. Aitken, E. K. Hege, and J. S. Morgan, "Triple-correlation subplane reconstruction of photon-address stellar images," *Journal of the Optical Society of America A*, vol. 7, pp. 1243–1250, Jul 1990.

[11] C. L. Matson, "Weighted-least-squares phase reconstruction from the bispectrum," *Journal of the Optical Society of America A*, vol. 8, pp. 1905–1913, Dec 1991.

[12] C. J. Carrano, "Progress in horizontal and slant-path imaging using speckle imaging," vol. 5001, pp. 56–64, SPIE, 2003.

[13] V. I. Tatarski, *Wave propagation in a turbulent medium*. New York: Dover, 1961.

[14] Y. I. J. C. Wyngaard and J. Stuart A. Collins, "Behavior of the refractive-index-structure parameter near the ground," *Journal of the Optical Society of America*, vol. 61, pp. 1646–1650, Dec 1971.

[15] W. A. Coles, J. P. Filice, R. G. Frehlich, and M. Yadlowsky, "Simulation of wave propagation in three-dimensional random media," *Applied Optics*, vol. 34, pp. 2089–2101, Apr 1995.

[16] J. M. Martin and S. M. Flatté, "Intensity images and statistics from numerical simulation of wave propagation in 3-d random media," *Applied Optics*, vol. 27, pp. 2111–2126, Jun 1988.

[17] S. M. Flatté and J. S. Gerber, "Irradiance-variance behavior by numerical simulation for plane-wave and spherical-wave optical propagation through strong turbulence," *Journal of the Optical Society of America A*, vol. 17, pp. 1092–1097, Jun 2000.

[18] M. C. Roggemann and B. Welsh, *Imaging through turbulence*. CRC Press, Boca Raton, FL, USA, 1995.

[19] A. V. Sergeyev, M. C. Roggemann, and C. Demars, "Near the ground laser communication system for monitoring the statistics of turbulence: fried parameter estimation from the psf measurements," vol. 7685, p. 76850L, SPIE, 2010.

[20] M. A. Vorontsov and G. W. Carhart, "Anisoplanatic imaging through turbulent media: image recovery by local information fusion from a set of short-exposure images," *Journal of Optical Society of America A*, vol. 18, pp. 1312–1324, Jun 2001.

[21] C. J. Carrano, "Anisoplanatic performance of horizontal-path speckle imaging," vol. 5162, pp. 14–27, SPIE, 2003.

[22] C. Macaskill and T. E. Ewart, "Computer simulation of two-dimensional random wave propagation," *IMA Journal of Applied Mathematics*, vol. 33, no. 1, pp. 1–15, 1984.

[23] D. L. Fried, "Anisoplanatism in adaptive optics," *Journal of the Optical Society of America*, vol. 72, pp. 52–52, Jan 1982.

[24] R. Rao, "Statistics of the fractal structure and phase singularity of a plane light wave propagation in atmospheric turbulence," *Applied Optics*, vol. 47, pp. 269–276, Jan 2008.

[25] J. W. Goodman, *Statistical optics*. Wiley-Interscience, New York, NY, USA, 1985.

[26] M. Wakin, "Lena512 standard test images.".

[27] J. P. Bos and M. C. Roggeman, "Simulation of extended scenes imaged through turbulence over horizontal paths," vol. 8161, p. 816106, SPIE, 2011.

[28] D. Fraser, G. Thorpe, and A. Lambert, "Atmospheric turbulence visualization with wide-area motion-blur restoration," *Journal of the Optical Society of America A*, vol. 16, pp. 1751–1758, Jul 1999.

[29] G. W. Carhart and M. A. Vorontsov, "Synthetic imaging: nonadaptive anisoplanatic image correction in atmospheric turbulence," *Optics Letters*, vol. 23, pp. 745–747, May 1998.

[30] C. J. Carrano, "Speckle imaging over horizontal paths," vol. 4825, pp. 109–120, SPIE, 2002.

[31] P. F. Curt, M. R. Bodnar, F. E. Ortiz, C. J. Carrano, and E. J. Kelmelis, "Real-time embedded atmospheric compensation for long-range imaging using the average bispectrum speckle method," vol. 7244, p. 724404, SPIE, 2009.

[32] Unknown, "Misc: Boats,the USC-SIPI image database.".

[33] D. L. Fried, "Limiting resolution looking down through the atmosphere," *Journal of the Optical Society of America*, vol. 56, pp. 1380–1384, Oct 1966.

[34] R. A. Muller and A. Buffington, "Real-time correction of atmospherically degraded telescope images through image sharpening," *Journal of the Optical Society of America*, vol. 64, pp. 1200–1210, Sep 1974.

[35] H. Tang, N. Joshi, and A. Kapoor, "Learning a blind measure of perceptual image quality," in *Computer Vision and Pattern Recognition (CVPR), 2011 IEEE Conference on*, pp. 305 –312, june 2011.

[36] A. Moorthy and A. Bovik, "A two-step framework for constructing blind image quality indices," *Signal Processing Letters, IEEE*, vol. 17, pp. 513 –516, may 2010.

[37] H. Sheikh, A. Bovik, and G. de Veciana, "An information fidelity criterion for image quality assessment using natural scene statistics," *Image Processing, IEEE Transactions on*, vol. 14, pp. 2117 –2128, dec. 2005.

[38] Z. Wang and A. Bovik, "Mean squared error: Love it or leave it? a new look at signal fidelity measures," *Signal Processing Magazine, IEEE*, vol. 26, pp. 98 –117, jan. 2009.

[39] S. Gabarda and G. Cristóbal, "Blind image quality assessment through anisotropy," *Journal of the Optical Society of America A*, vol. 24, pp. B42–B51, Dec 2007.

[40] J. P. Bos and M. C. Roggemann, "Mean squared error performance of speckle-imaging using the bispectrum in horizontal imaging applications," vol. 8056, p. 805603, SPIE, 2011.

[41] MATLAB, *version 7.12.0.635 (R2011a)*. Natick, Massachusetts: The MathWorks Inc., 2011.

[42] J. Goodman, *Introduction To Fourier Optics*. McGraw-Hill physical and quantum electronics series, Roberts & Company, 2005.

[43] M. Charnotskii, "Superresolution in dewarped anisoplanatic images," *Applied Optics*, vol. 47, pp. 5110–5116, Oct 2008.

[44] F. Roddier, J. M. Gilli, and J. Vernin, "On the isoplanatic patch size in stellar speckle interferometry," *Journal of Optics*, vol. 13, no. 2, p. 63, 1982.

[45] G. R. Ayers and J. C. Dainty, “Iterative blind deconvolution method and its applications,” *Optics Letters*, vol. 13, pp. 547–549, Jul 1988.

Appendix A

The "Boats" Data set

In Chapter 2 I developed a technique for simulating image formation over long horizontal paths. I also described the development of a 3000 frame horizontal imaging data set based on the "Lena" test image. Subsequently, that data set was used in Chapter 3 to evaluate the robustness of speckle imaging techniques applied to horizontal imaging scenarios. Since that works was originally completed a second data set based on the "Boats" [32] test image has been developed. All simulation parameters, including turbulence strength, imaging wavelength, aperture size, etc., were identical to those used to develop the "Lena" set as described in Chapter 2. Similarly, the data set features 1000 image frames for each turbulence condition totaling 3000 image frames. Example output frames from this data set and the diffraction-limited reference image are found in Fig.A.1. The MSE statistics for each turbulence condition over 1000 image frames are summarized in Table A.1. The

Table A.1
MSE statistics associated with the "Boats" data set.

Condition	MSE	σ_{MSE}
"Low"	440	80
"Moderate"	668	108
"Severe"	836	124

distribution of MSE counts across image frames was found to be distributed log-normally similar to the "Lena" data set. Comparing Table 3.1 and Table A.1 significant differences the mean values, μ_{MSE}, are noted, between the data sets, but the deviations, σ_{MSE} are very similar. In the case of the "Moderate" and "Severe" cases the deviations, σ_{MSE}, differed by only two counts. I suspect that the lower MSE counts in this second data set may be attributed to a relative lack of energy at higher spatial frequencies in the "Boats" image compared to the "Lena" image.

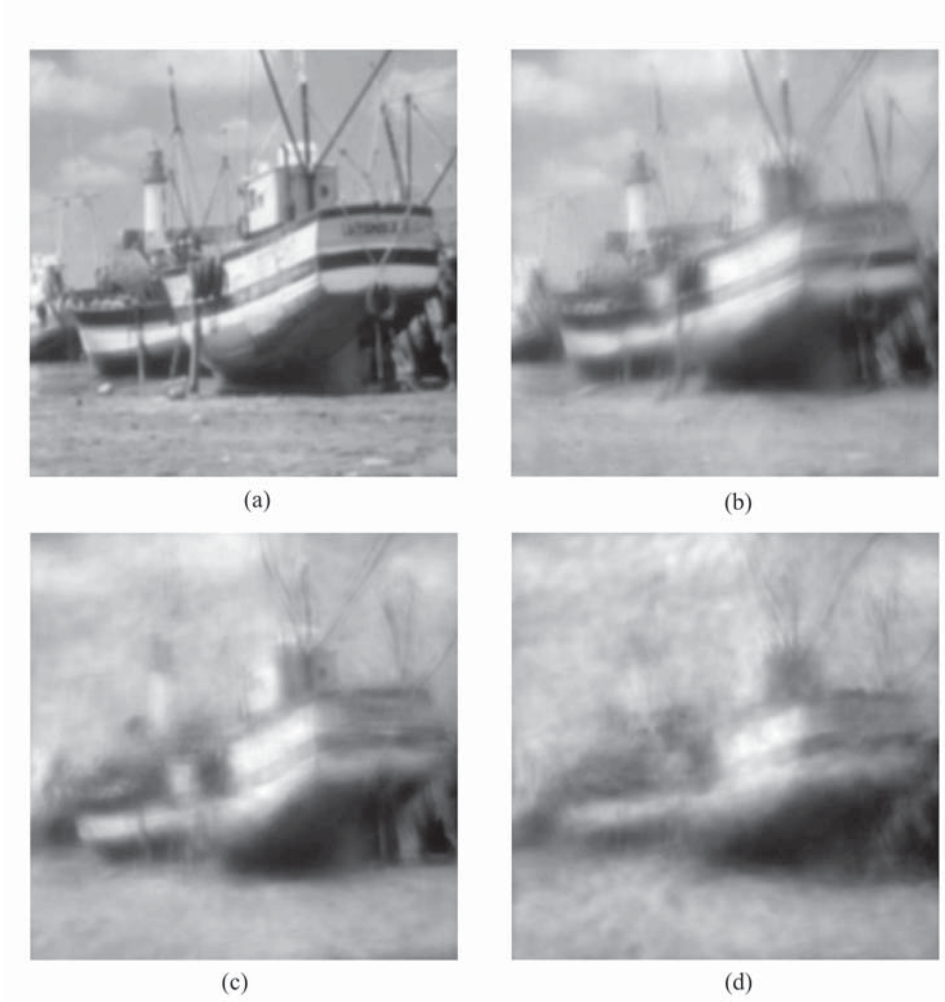

Figure A.1: Example frames from the "Boats" simulated data set. Image frames in the panel are for (a) diffraction-limited, (b)"Low", (c) "Moderate", and (d) "Severe" conditions.

Appendix B

Supplementary Analysis of "Boats" data set

The analysis in section 3.5 was repeated using the "Boats" derived data set in place of the "Lena" set. The sensitivity of residual MSE to variations in the parameters, α, C_n^2, N_f, and N_p was evaluated using the methods described in section 3.5 but excluded additive noise as a parameter for brevity. The results of this supplemental analysis are presented in Fig.B.1, Fig. B.2, Fig.B.3, and Fig.B.4. Example output frames following the recommendations presented in section 3.6 are found in Fig.B.5.

Comparing these results to their counterparts in section 3.5 only a few differences are worth noting. First, the optimum value of α was found to be $\alpha = 0.36$ using the "Boats" data set

Table B.1
Values of C_n^2 producing the minimum mean MSE in residual reconstruction MSE and the recorded deviation at that value.

Condition	Min. MSE	C_n^2 at Min. MSE $10^{-14}\mathrm{m}^{-2/3}$	Min. σ_{MMSE}
"Low"	133	1.3	6.4
"Moderate"	270	2.3	11.9
"Severe"	390	3.5	13.6

differing slightly from the $\alpha = 0.4$ found for the "Lena" data set. This optimum value for α was used in the evaluation of the remaining parameters. Next, referring to Table B.1, the values of C_n^2 that resulted in the minimum MSE are lower than theoretical values used by the simulation model by about 30 to 40% and are comparable to those found to be optimum for the original image set. In this case, MSE was reduced in the reconstruction frames by 53% on average compared to the inputs compared to the 48% observed for the same analysis in the using the "Lena" data set. The reductions in σ_{MSE} at the optimum value of C_n^2 were 89% on average over all turbulence conditions for both data sets. Also, as turbulence strength increased a similar reduction in sensitivity to variations in C_n^2 is observed. Comparing Fig.B.3 to Fig 3.6 and Fig. B.4 to Fig. 3.9 a nearly identical dependence of residual MSE to variations in parameters N_f and N_p is observed between data sets. Finally, as with the "Lena" data set the bispectrum and KT phase estimation methods provided equivalent results.

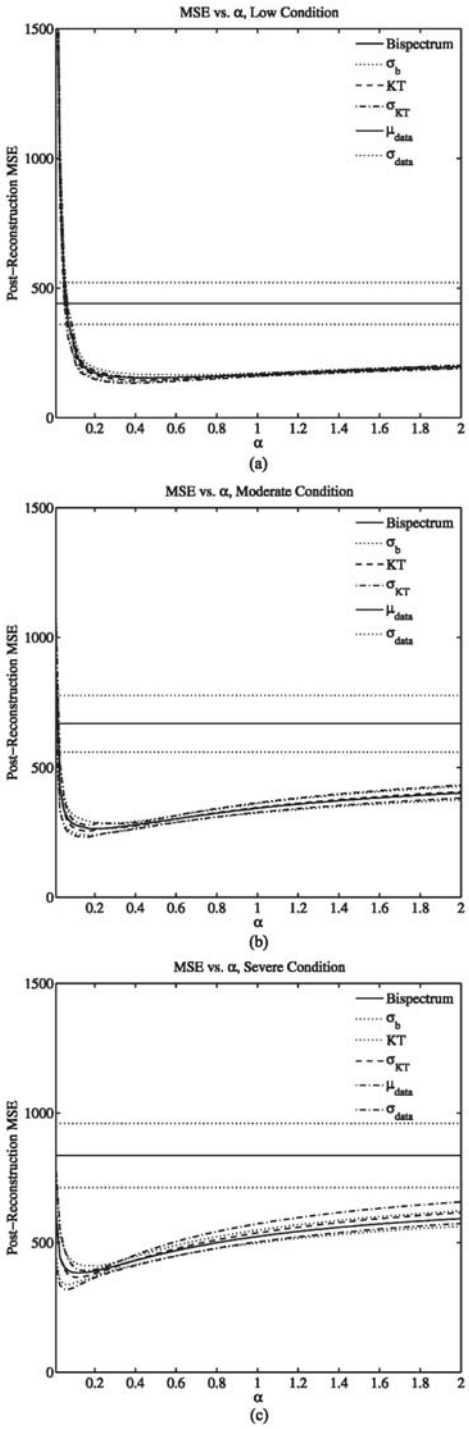

Figure B.1: Evaluation of the effect on the post-reconstruction residual MSE observed by varying α for the (a) "Low", (b) "Moderate", and (c) "Severe" turbulence conditions using the "Boats" data set as an input.

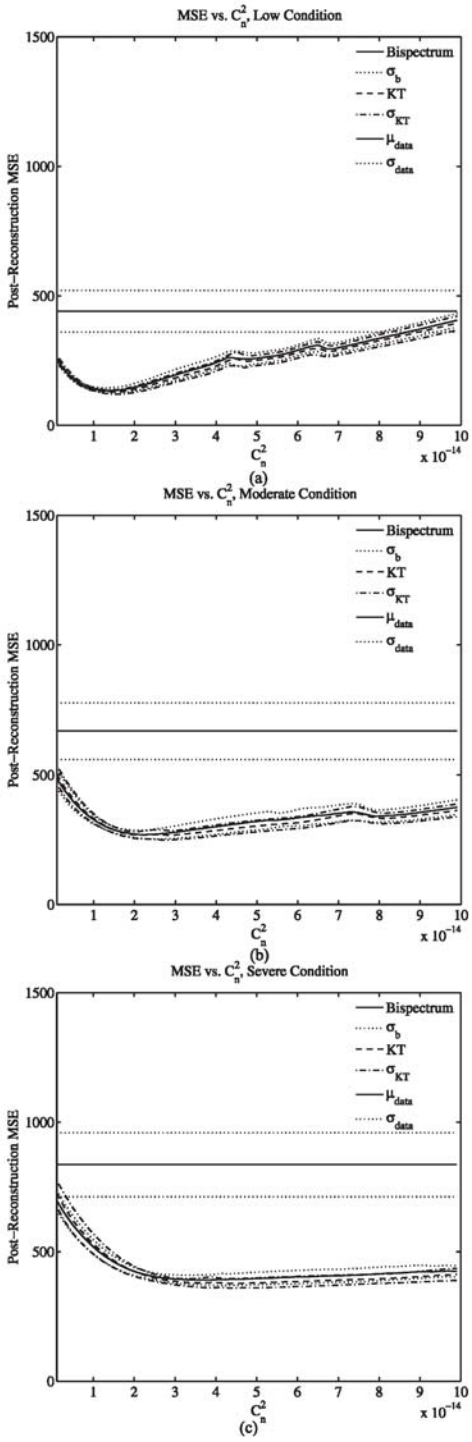

Figure B.2: Evaluation of the effect on the post-reconstruction residual MSE observed by varying C_n^2 for the (a)"Low", (b)"Moderate", and (c)"Severe" turbulence conditions using the "Boats" data set as an input.

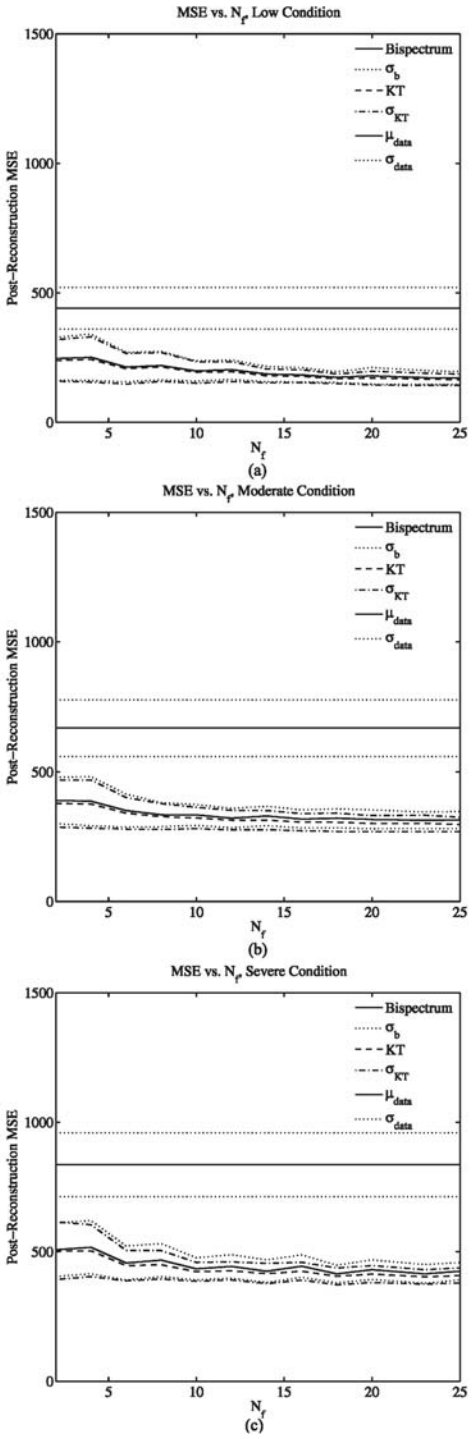

Figure B.3: Evaluation of the effect on post-reconstruction residual MSE observed by varying the number of input frames for the (a)"Low", (b)"Moderate", and (c)"Severe" turbulence conditions using the "Boats" data set as an input.

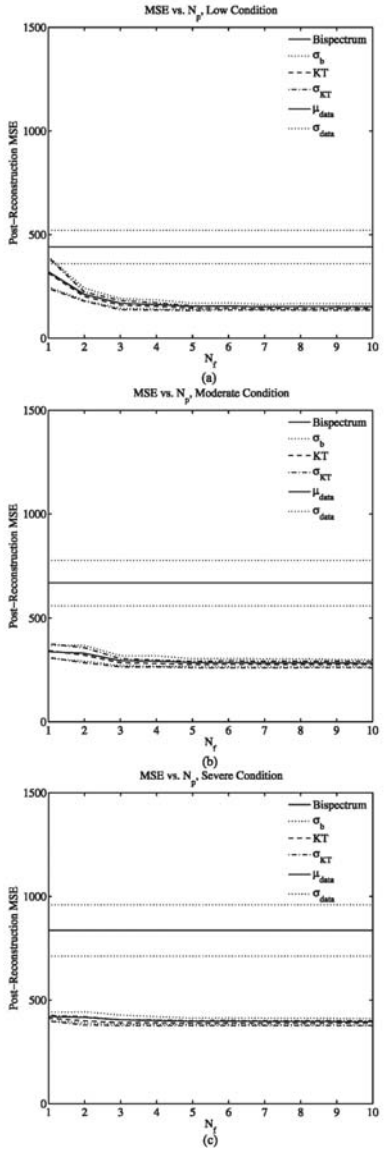

Figure B.4: Residual MSE as a function of the number of estimates, used to inform the estimated phase at each spatial frequency for the (a)"Low", (b)"Moderate", and (c)"Severe" turbulence cases using the "Boats" data set as an input.

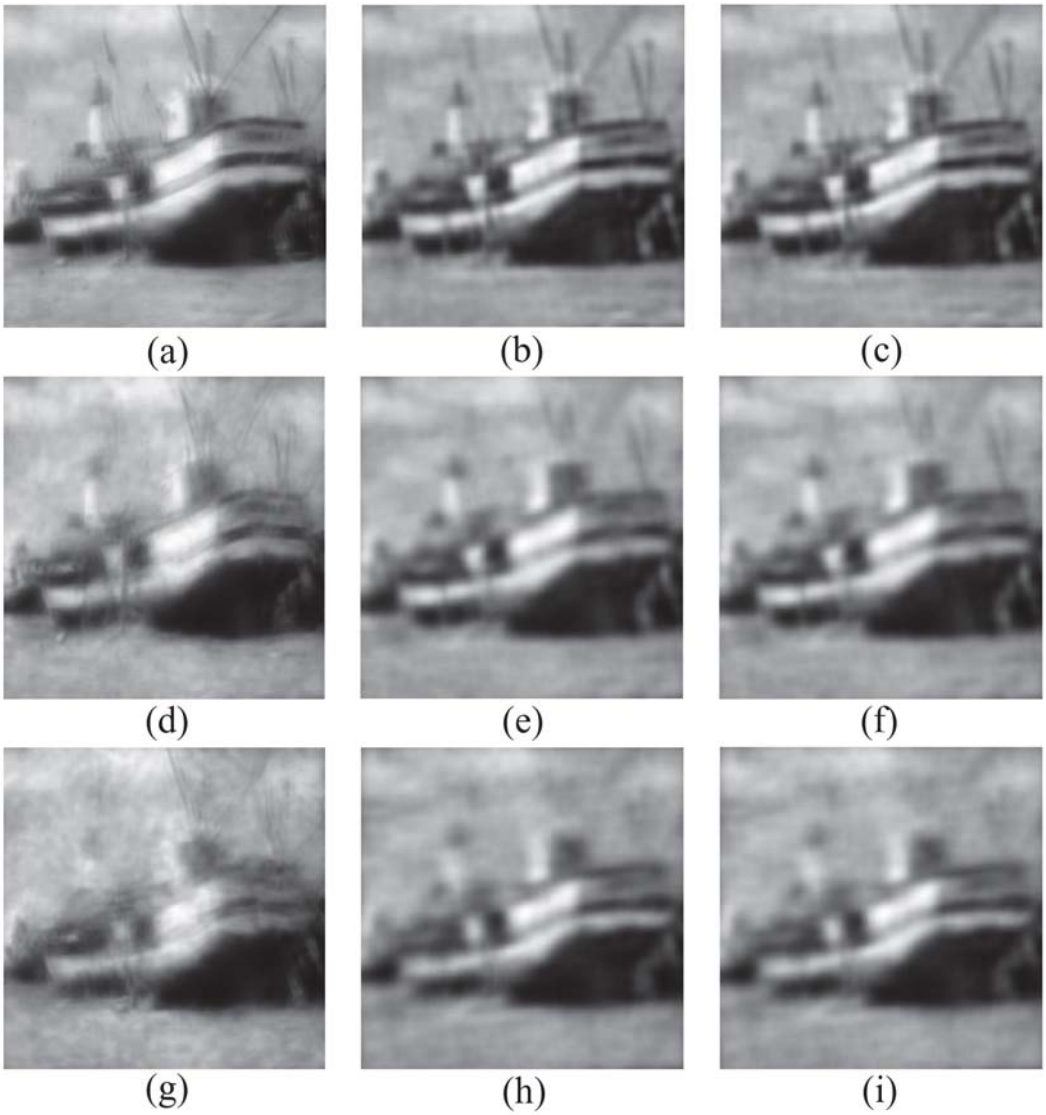

Figure B.5: Example input frames for the (a)"Low", (d)"Moderate", and (g)"Severe" turbulence cases from the "Boats" data set. Reconstructions using $N_f = 15$,$N_p = 4$,$\alpha = 0.4$, and the optimum values of C_n^2 listed in TableB.1 are presented for the bispectrum (b),(e),(h) and KT (c),(f),(i).

Appendix C

Letters of Permission

The content in Chapters 2, 3, and 4 have been published or are awaiting publication in SPIE Optical Engineering. Optical Engineering has the following policy regarding republication of this material:

> As stated in the SPIE Transfer of Copyright agreement, authors, or their employers in the case of works made for hire, retain the following rights: All proprietary rights other than copyright, including patent rights.
>
> - The right to make and distribute copies of the Paper for internal purposes.
> - The right to use the material for lecture or classroom purposes.
> - The right to prepare derivative publications based on the Paper, including books or book chapters, journal papers, and magazine articles, provided

that publication of a derivative work occurs subsequent to the official date of publication by SPIE.

Thus, authors may reproduce figures and text in new publications. The SPIE source publication should be referenced.